Geochemistry, Geophysics, Geosystems

RESEARCH ARTICLE
10.1029/2025GC012735

Key Points:

- Deep fluids outgassing from the Volcanic Eifel and the Ardennes have a common mantle origin
- The mantle CO_2 transported by groundwaters in the Eifel-Ardennes-Rhenish Massif is $7 \pm 4 \times 10^9$ mol yr^{-1}
- CO_2 degassing takes place between aquifer (4 bar, 160°C) and surface (1 bar, 9°C) conditions

Supporting Information:

Supporting Information may be found in the online version of this article.

Correspondence to:

L. Ricci,
lisa.ricci@collaboratori.unipg.it

Citation:

Ricci, L., Frondini, F., Morgavi, D., Caliro, S., Rizzo, A. L., Fischer, T. P., & Chiodini, G. (2026). A common mantle source for the endogenous CO_2 degassed at the Eifel (Western Germany) and the Ardennes (Eastern Belgium) regions. *Geochemistry, Geophysics, Geosystems*, *27*, e2025GC012735. https://doi.org/10.1029/2025GC012735

Received 10 OCT 2025
Accepted 17 MAR 2026

A Common Mantle Source for the Endogenous CO_2 Degassed at the Eifel (Western Germany) and the Ardennes (Eastern Belgium) Regions

Lisa Ricci[1], Francesco Frondini[1], Daniele Morgavi[2], Stefano Caliro[3], Andrea Luca Rizzo[4,5], Tobias P. Fischer[6], and Giovanni Chiodini[7]

[1]Dipartimento di Fisica e Geologia, Università di Perugia, Perugia, Italy, [2]Dipartimento di Scienze della Terra, dell'Ambiente e delle Risorse (DISTAR), Università Degli Studi di Napoli Federico II, Napoli, Italy, [3]Istituto Nazionale di Geofisica e Vulcanologia, Sezione di Napoli, Napoli, Italy, [4]Dipartimento di Scienze dell'Ambiente e della Terra, Università degli Studi di Milano-Bicocca, Milano, Italy, [5]Istituto Nazionale di Geofisica e Vulcanologia, Sezione di Milano, Milano, Italy, [6]Department of Earth Science, University of California, Santa Barbara, CA, USA, [7]Istituto Nazionale di Geofisica e Vulcanologia, Sezione di Bologna, Bologna, Italy

Abstract Tectonic CO_2 Earth degassing is globally relevant and has probably controlled climate on a geological scale (Brune et al., 2019, https://doi.org/10.1038/s41561-017-0003-6). Endogenous CO_2 outgassing from rifting areas remains poorly constrained, with most available data from the East African Rift. Here, we investigate the CO_2 degassing in the European Cenozoic Rift System (ECRIS), focusing on the chemical and isotopic composition of 161 springs emerging from the Eifel-Ardennes-Rhenish Massif region (Eastern Belgium-Western Germany). Theoretical water-gas-rock interaction models based on the chemistry of gases dissolved in East Eifel groundwaters reveal CO_2 efflux takes place in a P-T range between the aquifer depth (4 bar, 160°C) and spring emergence (1 bar, 9°C). He and C isotopes show that Ardennes, Volcanic Eifel and Rhenish Massif are all part of a unique degassing system. The average mantle CO_2 flux emitted from the region is $5 \pm 2 \times 10^6$ mol yr^{-1} km^{-2}, corresponding to a total deeply derived CO_2 emission rate of $7 \pm 4 \times 10^9$ mol yr^{-1}. These values are of the same magnitude as the global baseline defined for convective hydrothermal CO_2 emitted from areas of high heat flow, demonstrating the relevance of passive rifts as CO_2 emitters on a global scale.

Plain Language Summary Rifts, where the lithosphere is thinned by tectonic activity, are regions where the Earth naturally emits CO_2, but the quantification of these emissions is poorly constrained. Here, we quantify the CO_2 outgassing from the central sector of the European Cenozoic Rift System (ECRIS), which encompasses the Ardennes (Eastern Belgium), the Volcanic Eifel and the Rhenish Massif (Western Germany). CO_2 degassing was computed by studying the chemistry and the isotopic composition of 161 springs emerging from the region. CO_2 transported by groundwaters originated in the mantle and is 7 billion moles per year (which means 0.3 megatons per year). The corresponding CO_2 flux, expressing the quantity of CO_2 annually emitted per km^2, is 5 million moles annually emitted per km^2. Theoretical models reveal the CO_2 release takes place between the aquifer depth (where P is 4 bar and T is 160°C) and the emergence of springs at surface (P = 1 bar and T = 9°C). Finally, this study demonstrates that the gases emitted from the Volcanic Eifel, the Ardennes and the Rhenish Massif have a common origin. This means that the three areas belong to a unique degassing system, with deep fluids able to migrate through faults and fractures.

1. Introduction

Continental rifts are characterized by CO_2 degassing, occurring as diffuse emissions from soil (Cappelli et al., 2023; Hunt et al., 2017; Lee et al., 2016), dry gas vents (Bräuer et al., 2013; Gal et al., 2018; Kämpf et al., 2019; Weinlich et al., 1999), CO_2-rich bubbling springs (Boudoire et al., 2025; Griesshaber et al., 1992; Ricci et al., 2024; Weinlich et al., 1999) and efflux from volcanic lakes (Pérez et al., 2011; Rafflin et al., 2024). In the Rhine rift system, the central sector of the European Cenozoic Rift System (ECRIS), volatile outgassing occurs over a large area that includes the Rhenish Massif, the Rhine Graben and the Black Forest. In the Rhenish Massif, several CO_2-rich mineral springs, dry gas vents (i.e., the Laacher See and Wehrer Kessel mofetes, Van Daele & Ferket, 2021) and cold CO_2 geysers (i.e., Andernach geyser, Van Overmeeren, 2014) are distributed along the major tectonic structures (e.g., the Siegen Main Thrust) and at the contact between the Devonian basement and the overlying volcanic formations. In this study, we investigate the geochemistry of 161 springwaters emerging across an area of approximately 1,600 km^2 encompassing the Volcanic Eifel, the Rhenish Massif *sensu strictu* and the Ardennes, with the aim to (a) unravel the origin of the circulating fluids and released volatiles, (b) model the degassing process and (c) estimate the CO_2 flux emitted from the area. Furthermore, we provide the first data set on the chemical composition of dissolved gases for eight springwaters emerging from the Volcanic Eifel, from which we derived a water-gas-rock interaction model to constrain the degassing process affecting the area.

The Volcanic Eifel (Western Germany) is a Quaternary volcanic complex active between 700 ka and 11 ka. Volcanological studies have devoted particular attention to the Laacher See Volcano (East Eifel), which gave rise to one of the major prehistoric Plinian eruptions (12,900 ya) of highly evolved magma of central and southern Europe (Schmincke et al., 1999), witnessed by the Laacher See maar lake. At present, the Volcanic Eifel is a dormant province, with widespread CO_2-rich gas emissions, weak earthquakes and deep low-frequency seismic events as evidence of an unfinished magmatic activity (Rizzo et al., 2021 and references therein, Ritter et al., 2024). The origin of magmatism in the Eifel is a matter of debate, with particular focus being on whether there is a mantle plume beneath the area (Bekaert et al., 2019; Bräuer et al., 2013; Caracausi et al., 2016; Moreira et al., 2018; Ritter et al., 2001; Rizzo et al., 2021), resulting in different genetic models of the Central European Volcanic Province (CEVP).

The Rhenish Massif, underlying the Volcanic Eifel, is a basement of Devonian age, strongly folded by the Hercynian orogeny. Analogously to what has been observed in the French Massif Central and in the Bohemian Massif, the development of ECRIS has induced the reactivation of Variscan crustal fractures permeating the massifs (Dèzes et al., 2004; Schumacher, 2002) and is currently acting as an efficient pathway for fluid migration (Ricci et al., 2024; Tamburello et al., 2018). A similar tectonic setting characterizes the Ardennes (Eastern Belgium), which are Devono-Carboniferous sandstones and limestones (Barros et al., 2021) that overtops the western sector of the Rhenish Massif, where ENE-WSW to E-W longitudinal folds and thrust faults are cut by several NNW-SSE trending faults (Demoulin, 1998). Here, several CO_2-rich springs known from historical age, as the worldwide famous Spa thermal waters, emerge along structural discontinuities and faults (e.g., the Midi-Aechean fault, Hence et al., 1999). This paper provides geochemical constraints on the possible common origin of fluids degassed at the Eifel and the Ardennes domains and quantifies the average mantle-derived CO_2 degassing from the whole Eifel-Ardennes-Rhenish Massif area.

2. Geological and Hydrogeological Setting

The study area (Figure 1) is located at the Rhenish Massif, an uplifted plateau composed of Devonian and Carboniferous low-grade metamorphic and sedimentary rocks, strongly folded by the Variscan orogeny (Illies & Greiner, 1979). Volcanic Eifel (central-western Germany and eastern side of the study area, Figure 1) is a Quaternary volcanic field overlying the Rhenish Massif, whose development is linked with the evolution of the ECRIS system. Volcanic Eifel is a set of two volcanic provinces: West Eifel and East Eifel. West Eifel (600 km^2, Schmincke, 2007) comprises approximately 240 volcanoes, which mainly erupted primitive, silica-undersaturated alkali-rich magmas (foidites, olivine nephelinites and basanites, Duda & Schmincke, 1985) between 700 and 10.9 ka (Schmincke, 2007; Schmincke et al., 1983; Zolitschka et al., 1995). Here, some eruptive centers, now maars, brought ultramafic mantle xenoliths to surface (Aulbach et al., 2020; Shaw, 2004; Shaw et al., 2018). East Eifel (400 km^2, Schmincke, 2007) is constituted of about 100 volcanoes which erupted between 460 and 12.9 ka (Schmincke, 2007), producing a wide range of magmatic compositions (e.g., nephelinites, basanites, tephrites, phonolites, trachytes, Schmincke, 2007). More evolved magmas mainly erupted from three volcanic centers: Rieden (430–360 ka, phonolitic, Schmincke, 2007; Sundermeyer et al., 2020), Wehr (215–190 ka, phonolitic and trachytic, Wörner et al., 1988; Sundermeyer et al., 2020), and the VEI 6 Laacher See eruption, which is also the last volcanic episode of East Eifel (12.9 ka, Sundermeyer et al., 2020; Wörner & Schmincke, 1984). Besides silicic magmas, rare occurrences of carbonatites were recorded in the Volcanic Eifel. In the West Eifel, the only known carbonatitic volcanism is at Auf Dickel diatreme, in the Rockeskyll complex (Riley et al., 1996, 1999); in the East Eifel, carbonatites are locally found as rare clasts of intrusive syenite-carbonatite in the Laacher See phonolites (Schmitt et al., 2010, 2017) and as zeolitic-carbonatitic binding phase at Rieden (Hunger et al., 2024). Within the two volcanic fields, the distribution of volcanoes follows a NW-SE trend (Dahm et al., 2020), driven by preexisting lithospheric structures/discontinuities inherited by the Variscan collision and reactivated during the rifting stage (Mertes & Schmincke, 1985). This orientation is

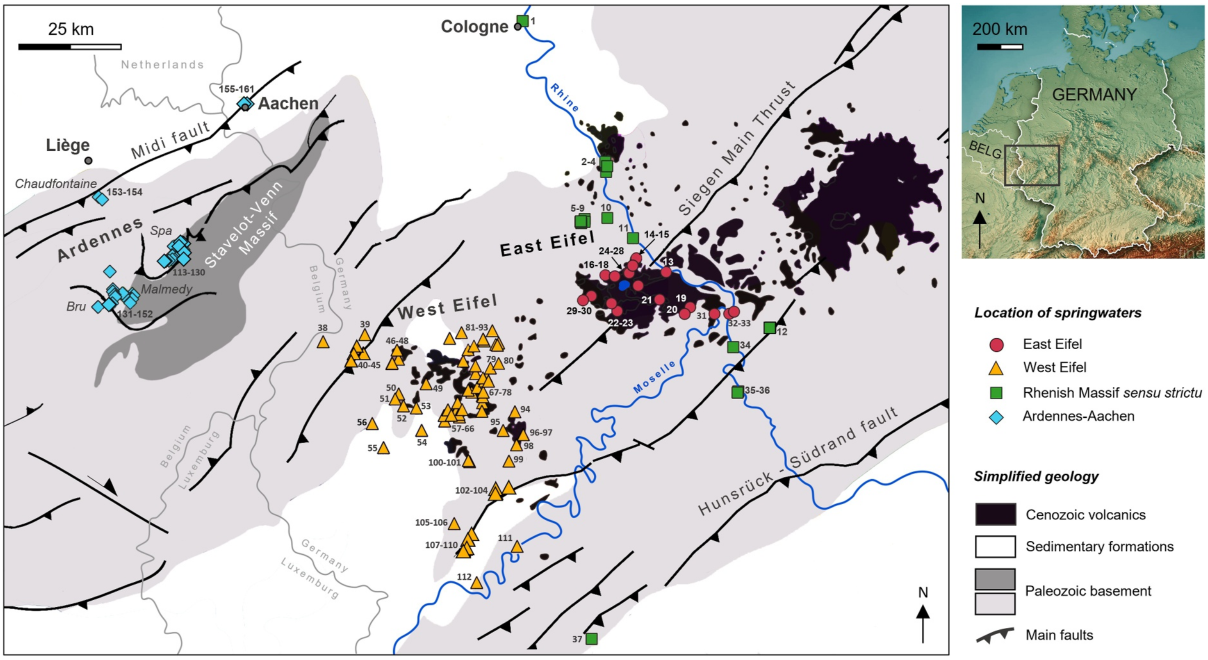

Figure 1. Location of the springwaters and simplified geological-tectonic setting of the study area, modified after Barros et al. (2021). East Eifel springs, red dots; West Eifel springs, yellow triangles; Rhenish Massif *sensu strictu* springs, green squares; Ardennes-Aachen springs, light blue diamonds. The symbology here introduced is adopted throughout.

perpendicular to the NE-SW main tectonic lineaments of the area (i.e., Siegen Main Thrust, Hunsrück-Südrand fault) and to the direction of maximum horizontal extension (May et al., 1996). Regional tectonics also affect the spatial distribution of springwaters, which emerge from the Quaternary volcanics or from the Devonian basement, mainly along the NW-SE normal faults or the N-S or E-W strike-slip faults (May et al., 1996; Van-Den-Boom & Krimmel, 1986). Water flow circulation occurs both at shallow levels (e.g., in the volcanics and/or in the sedimentary cover, May et al., 1996) and at depth in the basement. Deeper circulation is allowed and promoted by hydraulically conductive faults, which enhance water inflow and ascent (May et al., 1996). The study area also comprises the Ardennes and Aachen. The Ardennes (southern Belgium and western side of the study area, Figure 1) are the Belgian sector of the Rhenish Massif, composed of Cambro-Ordovician basements overlapped by Devono-Carboniferous sandstones and limestones (Barros et al., 2021). The studied springs are located in the eastern Ardennes, south of Liege, within the Stavelot-Venn Massif, a siliciclastic sedimentary sequence of Cambro-Ordovican slates and quartzites constituting the basement, upon which Devonian to Carboniferous quartzites, sandstones, conglomerates and siltstones are superimposed (Barros et al., 2021). Chaudfontaine (samples 153–154) is northward of the Stavelot-Venn Massif, along the Midi fault Zone, a major thrust extending for 100 km in length and 15 km in depth (DEKORP Research Group, 1991) which borders the NW sector of the Rhenish Massif. The hydrogeological setting of the Ardennes study area is strongly linked to the presence of faults, joints and discontinuity boundaries (Barros et al., 2021): deep aquifers are hosted in fractured quartzites and sandstones and their extension and permeability are largely controlled by the fracture networks (Barros et al., 2021). Shallow, unconfined aquifers locally occur at the boundary between quartzites and the less permeable shales and or slates (Barros et al., 2021). The spatial distribution of springwaters is intrinsically linked to the fault geometry, which drives fluid circulation. Aachen is placed on the border between the Rhenish Massif and the Lower Rhine Graben. Springs emerge at the intersection between NE-SW thrust systems (i.e., the Midi Thrust and the Burtscheid Thrust faults, Gómez-Díaz et al., 2025) and NW-SE faults (e.g., the Lousberg fault, Gómez-Díaz et al., 2025). Seismic reflection data revealed a SE-dipping reflector, extending for about 80 km from the Ardennes to the northern West Eifel, reaching a depth of 12 km. This reflective zone corresponds to the basal detachment of the Eifel fold and thrust belt, the northwestern front of the Rhenish Massif (Eickhoff et al., 2025). In the following sections, the geochemical data from the Eifel-Ardennes-Rhenish Massif springwaters will be treated maintaining the groups showed in Figure 1, in detail: East Eifel springwaters (samples 13 to 33, red dots), West Eifel springwaters (samples 38 to 112, yellow triangles); Rhenish Massif *sensu strictu* springwaters (samples 1 to 12 and 34 to 37, including also the Cologne spring, sample 1, located in the lower Rhine Graben, green squares) and the Ardennes-Aachen springwaters (samples 113 to 161, light blue diamonds).

3. Materials and Methods

3.1. Groundwater Sampling and Analysis

Groundwater from 13 springs emerging in the East Eifel (Eifel Volcanic Field) were collected in July 2022. Temperature, pH, Eh and electrical conductivity (EC) were measured directly in the field by using WTW pH-Eh/cond 3320 multi-meter. The HCO_3^- content was measured in the field through acid titration with HCl 0.01 N, using methyl orange as indicator (error = 1%). Water samples for chemical and isotopic (δD, $\delta^{18}O$) analyses were collected in 100 ml polyethylene bottles. The water aliquot for anion determination was filtered through 0.45 μm membrane filters while the water aliquots for cations were filtered and immediately acidified with 1% of 1:1 diluted HCl. Water samples for the determination of the isotopic composition of total dissolved inorganic carbon ($\delta^{13}C_{TDIC}$) were collected in 1,000 or 500 ml polyethylene bottles, depending on the expected bicarbonate content. The dissolved carbon was precipitated directly in the field as $SrCO_3$, by adding $SrCl_2$ and NaOH to the water sample. In the laboratory, the precipitated carbonates were then filtered, washed with distilled water and dried in a N_2 atmosphere. Dissolved gases (CO_2, N_2, O_2, Ar, He, CH_4) were sampled on eight Eifel springs using pre-evacuated 250 ml glass vials equipped with a three-way glass valve or a Thorion valve, filling the sampler up to 65%–80% (V_{liq}) of its volume (V_{tot}), following the methodology described by Chiodini (1996) and Caliro et al. (2005).

Major dissolved ions were determined at the geochemical laboratory of the Department of Physics and Geology of Perugia University. Ca and Mg concentrations were determined by atomic absorption (AA) flame spectroscopy while Na, K and Li were determined by atomic emission (AE) flame spectroscopy, using an IL 951 AA/AE spectrometer. Cl, SO_4, NO_3 and F were determined by ion chromatography, using a Dionex DX-120 Ion Chromatograph. Carbon, oxygen and hydrogen isotopes analyses were performed by means of standard mass spectrometry techniques at the Geochemistry Laboratory of the Istituto Nazionale di Geofisica e Vulcanologia-Osservatorio Vesuviano (INGV-OV) of Napoli, using a Finnigan Delta plusXP continuous flow mass spectrometer (MS) coupled with a GasbenchII device (GBII) (analytical errors: δD ± 1‰, $\delta^{18}O$ ± 0.08‰ and $\delta^{13}C$ ± 0.06‰). Isotopic compositions are given in δ‰ notation per mill versus V-PDB for carbon and versus V-SMOW for oxygen and hydrogen. The dissolved gas phase, separated in the headspace of the vial ($V_{gas} = V_{tot} - V_{liq}$), was analyzed by a gas chromatograph equipped with a Thermal Conductivity (TCD) detector, following Chiodini (1996) and Caliro et al. (2005), using He as carrier gas. The partial pressure of each gas species (CO_2, N_2, O_2, Ar and CH_4) was determined with reference to standards at different pressures. He partial pressures were determined in the same injection by a leak detector (detection limit 0.00015 mbar).

3.2. The Geochemical Data Set

The data collected in this study (13 springs from the East Eifel) were integrated with bibliographic data to construct the Eifel-Ardennes-Rhenish Massif data set.

The Eifel-Ardennes-Rhenish Massif data set (Ricci et al., 2026) is constituted by the chemical analysis of 161 water samples, the water isotopic composition ($\delta^{18}O$ ‰, δD ‰) of 31 samples, the carbon isotopic composition ($\delta^{13}C_{TDIC}$ ‰) of 47 water samples and the composition of gases dissolved in 8 water samples. The analytical error of the data set, evaluated by checking the charge balance, is lower than 3% for 54% of samples and is 5% on average.

3.3. Aqueous Speciation and Geochemical Modeling

The speciation of the solutions, the total dissolved inorganic carbon (TDIC), the partial pressure of carbon dioxide (pCO_2) and the saturation indexes of calcite for each studied groundwater (Ricci et al., 2026) were computed through the PHREEQC version 3 code (Parkhurst & Appelo, 2013), using the llnl.dat thermodynamic database (Delany & Lundeen, 1990; Wolery, 1979, 1992; Wolery & Jarek, 2003). The PHREEQC version 3 code was also used to compute the theoretical water-gas-rock interaction models describing the evolution of infiltrating water as it interacts with a deep gas phase and the host rocks, following the methodology described by Caliro et al. (2005) and Ricci et al. (2024).

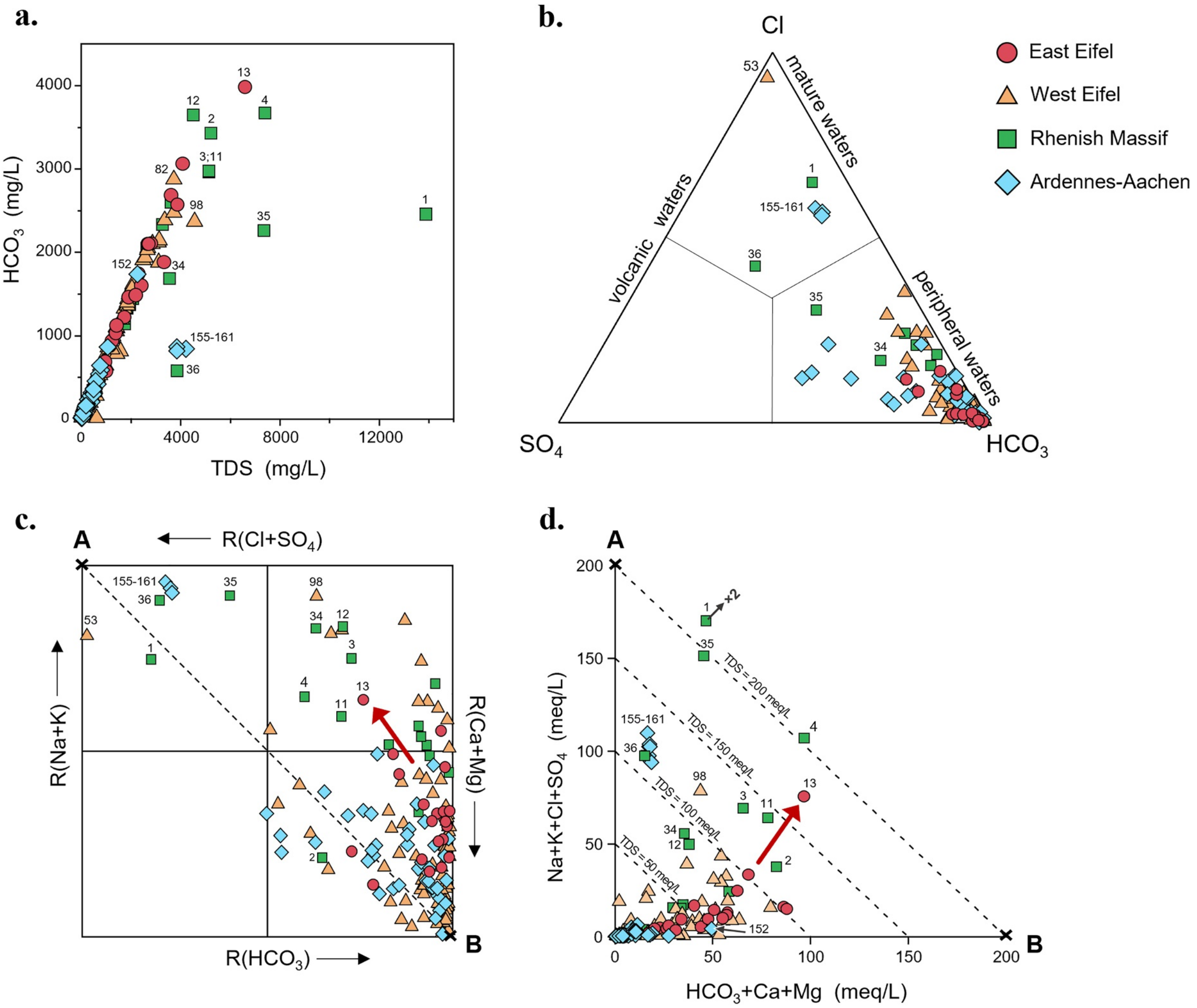

Figure 2. (a) Binary plot of the total dissolved solids versus bicarbonate content of groundwaters; (b) Cl-SO_4-HCO_3 ternary diagram (Giggenbach & Goguel, 1989); (c) Langelier-Ludwig diagram; (d) Salinity section in the A-B transect of the Langelier-Ludwig diagram. Red arrows indicate the evolution of East Eifel waters toward the composition of Andernach (sample 13).

4. Results

4.1. Chemical Composition of Waters

At emergence, the investigated springwaters (13 new data, 148 literature data, Ricci et al., 2026) exhibit temperatures between 5 and 72°C, 16°C on average. Most of the studied waters (approximately 75%) have temperatures close to the average land surface air temperature of the region ($T = 9.68°C$, Climate Change Knowledge Portal, 2025) or slightly higher, while the remaining 25% of samples have temperatures ranging from 15 to 72°C. Waters with higher temperatures generally emerge from the fractured basement, such as Bad Neuenahr springs (samples 5 to 9, $23 < T < 42°C$), Lahnstein spring (sample 34, $T = 38°C$) and Bad Ems borehole (sample 12; $T = 40°C$) or along major faults, such as Chaudfontaine springs (samples 153 and 154, $T = 32°C$ and 24°C, respectively) and Aechean springs (samples 155 to 161, with T between 39 and 72°C). The total dissolved solids (TDS) ranged between 18 and 13,887 mg L^{-1} (1,625 mg L^{-1} on average), with almost half of the samples having TDS >1,000 mg L^{-1}. The pH values range between 4.3 and 8.9, pH = 6.2 on average; most of waters (80%) are acidic (pH < 7) and almost half of samples show a pH between 5.5 and 6.5.

Bicarbonate is the most abundant ion and shows a good correlation with the TDS ($R^2 = 0.70$, Figure 2a).

The Cl-SO_4-HCO_3 diagram (Giggenbach & Goguel, 1989; Figure 2b) shows that most of the samples are "peripheral waters," distributed along a trend pointing toward the range of "mature waters." Only a few samples fall within the "mature waters" domain: Densborn (sample 53, the most acidic water of the data set, with pH = 4.3), Aachen springs (showing the highest temperatures of the data set) and Cologne (sample 1) spring, a highly saline (TDS = 13,887 mg L^{-1}) and slightly acidic (pH = 6.1) Na-Cl water.

The Langelier-Ludwig diagram (Langelier & Ludwig, 1942; Figure 2c) shows that the majority of samples (79%) are bicarbonate-Earth alkaline waters, the 14% are bicarbonate–alkaline waters and the remaining samples (7%) are chloride-alkaline waters.

Bicarbonate-alkaline and chloride-alkaline waters are characterized by a high salinity (TDS >1,440 mg L^{-1}), while bicarbonate-Earth alkaline waters are associated with both high and low TDS contents. Most springs with a thermal footprint fall in the range of bicarbonate-alkaline waters, with the exception of Chaudfontaine springs, which plot in the bicarbonate-Earth alkaline domain (as almost all the Ardennes groundwaters) and Aechean springs that have chloride-alkaline composition.

East and West Eifel samples are both bicarbonate-alkaline and bicarbonate-Earth alkaline waters, with East Eifel waters roughly aligned along a trend pointing toward Andernach (sample 13, Figure 2c), the water with the highest HCO_3 content of the study area (Figure 2a). The salinity section (Figure 2d) slightly shows the same trend.

Aachen springs are characterized by a TDS ranging between 3,832 and 4,426 mg L^{-1}, markedly higher than the TDS of the majority of Ardennes springwaters (442 mg L^{-1} on average). Figure 2d clearly shows that these Na-Cl waters do not align on the same trend on the Ardennes samples.

4.2. Estimation of Reservoir Temperatures

In order to estimate the temperature at aquifer conditions, water maturity was first evaluated (Supporting Information S1). Most solutions (94% of samples) are immature; thus, their composition is controlled by rock dissolution rather than equilibration (Giggenbach, 1988). This makes these waters unsuitable for temperature estimation based on Na/K and K/Mg cation geothermometers (Giggenbach, 1988). The remaining solutions are partially equilibrated, showing dilution effects, and are suitable for the application of the Na/K geothermometer. These waters are Aachen springs (sample 155 and 161) and three Rhenish Massif *sensu strictu* springs (samples 1, 35 and 36). The effects of dilution or mixing with low ionic strength solution on water maturity, following Romano and Liotta (2020), are detailed discussed in Supporting Information S1. The computed aquifer temperatures by means of the Na/K geothermometer (Giggenbach, 1988) are between 127 and 142°C for Rhenish Massif *sensu strictu* waters and between 182 and 201°C for Aachen springwaters. Regarding SiO_2 polymorphs, the speciation of groundwater samples where the SiO_2 concentration is known (i.e., West Eifel springs, Ardennes-Aachen waters and two Rhenish Massif *sensu strictu* waters, which are samples 10 and 11) reveal that all these solutions are oversaturated with quartz and chalcedony at emergence and undersaturated with amorphous silica. Quartz geothermometry (Fournier & Potter, 1982) applied to these waters by correcting for dilution effects confirms the results computed with the Na/K ionic geothermometer, highlighting temperatures up to 200°C.

4.3. Stable Isotopes of Water

The isotopic composition of stable isotopes of waters (δD-$\delta^{18}O$ plot, 13 East Eifel data from this work, 18 Ardennes data from literature; Ricci et al., 2026) is shown in Figure 3. The δD values are comprised between −71.4‰ and −50.6‰, while the $\delta^{18}O$ ranges from −9.7‰ to −7.3‰. Most of the samples fall along or between the global meteoric water line (GMWL; Craig, 1961) and the regional meteoric water line (RMWL; Stumpp et al., 2014). The deuterium excess, *d,* is a second order parameter reflecting non-equilibrium isotope fractionation during evaporation ($d = \delta D - 8\delta^{18}O$; Dansgaard, 1964) and depending on sea surface temperature and relative humidity. Our data show a *d* between 5.6 and 10.7‰ (8.0‰ on average), falling in the range of predicted evaporation *d* for the northern hemisphere (Pfahl & Sodemann, 2014). The only exception is sample 32, characterized by a lower deuterium excess (*d* = 2.2‰), likely related to evaporation after spring emergence.

Based on the oxygen isotopic composition of Koblenz rainwater ($\delta^{18}O = -7$‰, Stumpp et al., 2014), the average altitude of Koblenz (73 m a.s.l.) and the global average elevation gradient (−2.8‰/km, Kern et al., 2020), the altitudes of the recharge area have been computed to be between 180 and 860 m a.s.l., in agreement with the maximum altitudes of Volcanic Eifel (Hohe Acht, 747 m a.s.l.) and Ardennes (Signal de Botrange, 694 m a.s.l.).

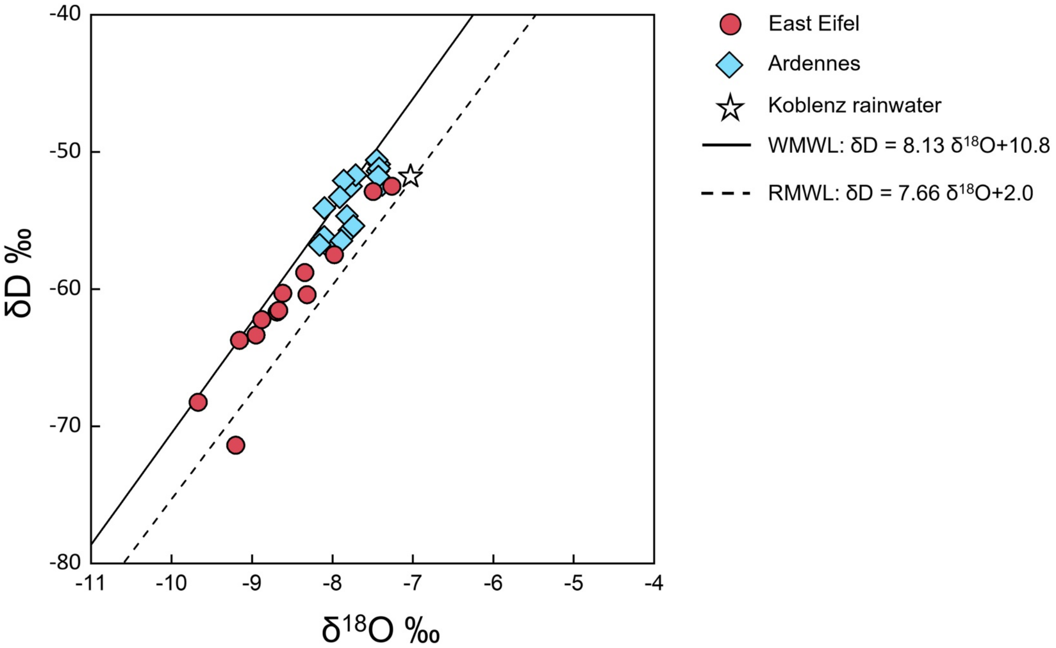

Figure 3. δD versus δ^{18}O plot. Solid line is the World Meteoric Water Line (WMWL, Craig, 1961); dashed line is the Regional Meteoric Water Line (RMWL, Stumpp et al., 2014). The isotopic composition of Koblenz rainwater (open star, Stumpp et al., 2014) is shown as a reference. East Eifel data are from this work, Ardennes data are from Griesshaber et al. (1992), Barros et al. (2021), Defourny et al. (2022), Gómez-Díaz et al. (2025), and references therein.

4.4. Dissolved Gases

Eight East Eifel springs were sampled in July 2022 to determine the chemical composition of the dissolved gases (Ricci et al., 2026). The content of non-reactive gaseous species He, Ar and N_2 is shown in the ternary diagram of Figure 4.

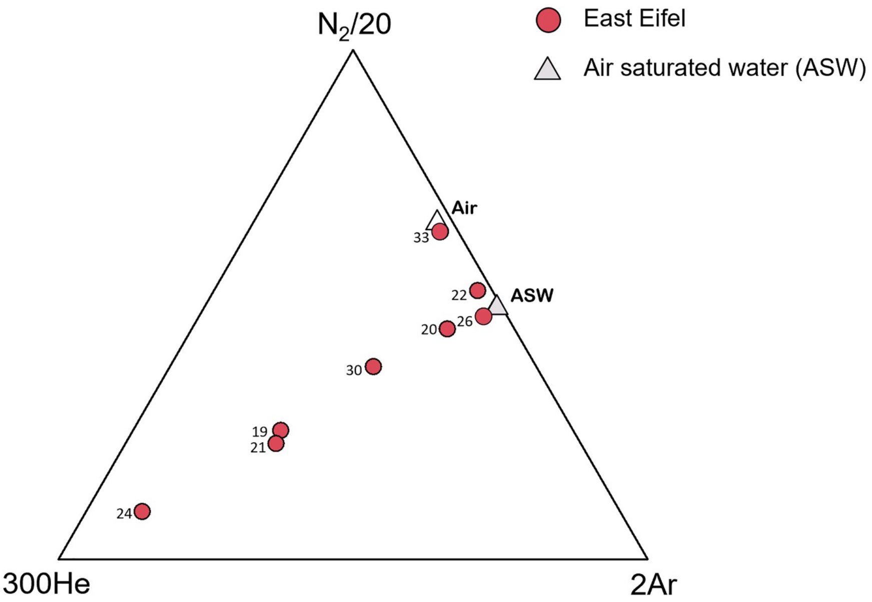

Figure 4. Ternary diagram of relative abundances of Ar-N_2-He in East Eifel samples, showing also the composition of air saturated water (ASW, gray triangle) and air (open triangle).

Here, as a reference, the compositions of air and of air-saturated water (ASW) are reported. ASW was computed using the PHREEQC version 3 code by equilibrating meteoric water from the study area (Deuselbach rainwater, Krämer et al., 1996) with the atmosphere. In practice, this corresponds to equilibrate the solution with the atmospheric partial pressures of Ar, CO_2, He and N_2.

Figure 4 shows that most samples align along a trend between the ASW and a He-rich endmember. Only sample 22 slightly deviates from this trend, falling between the composition of the ASW and of air and sample 33, having almost the same Ar-N_2-He relative abundances of air.

To interpret the chemical composition of gases dissolved in springwaters, data are compared to three theoretical models, defined by Caliro et al. (2005) and Ricci et al. (2024), that simulate the evolution of a meteoric water progressively interacting with the deep gas (DG) and the host rocks (Figures 5a and 5b).

The DG consists of a mixture of CO_2, He, Ar and N_2. The definition of the DG, the host rock and the three theoretical water-gas-rock interaction models (Model 1, Model 2, Model 3) are described in detail in Supporting Information S1. Model 1 (Figure 5a) is obtained by adding the DG to the ASW assuming the absence of CO_2 degassing and calcite precipitation (*no sink* condition, Chiodini et al., 2000). In Model 1, the confining pressure is always higher than the gas pressure; therefore, degassing is prevented. Model 2 is implemented assuming continuous degassing at 1 bar and 9°C, which practically means setting the total gas pressure at 1 bar and the temperature of the system at 9°C during the progressive addition of the DG and the concomitant dissolution of the volcanic glass. This model simulates the *P-T* condition corresponding to the aquifer-atmosphere interface. Model 3 is performed with the aim to simulate the degassing under aquifer conditions. This model is implemented analogously to Model 2, with the difference that, in Model 3, the addition of the DG and the dissolution of the volcanic glass to the ASW were simulated by setting the total gas pressure at 4 bar and the temperature of the system at 160°C. The *P* of Model 3 (4 bar) is the maximum pCO_2 at which the studied samples equilibrate with calcite, under the assumption that solutions oversaturated with calcite at the surface were at least in equilibrium with this mineral prior to CO_2 degassing; the *T* of Model 3 (160°C) is the average temperature of the reservoir computed with the K-Na cation geothermometer (see Section 4.2).

In Models 2 and 3, the incremental addition of the DG induces the progressive degassing of the solution and the precipitation of calcite. At each addition step, the number of the dissolved species, the exsolved gases and the precipitated calcite have been computed.

In Figure 5a, the theoretical models are compared to the dissolved gas composition of Eifel waters. Model 1 (dashed line in Figure 5a) is a binary mixing between the ASW and the DG and is unable to constrain the dissolved gas data. Model 2 (blue curve in Figure 5a) and Model 3 (pink curve in Figure 5a) both show a hyperbolic trend due to the different solubilities of Ar, He, and CO_2 in water. Ar and He preferentially exsolve before CO_2, which is stable as dissolved in water up to a higher amount of added DG and reacts with the volcanic glass. When pCO_2 equals the total gas pressure, the water system begins to degas CO_2. This drives the evolution of Models 2 and 3 toward CO_2 apex. Sample 19, 21 and 30 are better explained by Model 2, while sample 24 is accurately interpolated by Model 3. The composition of the remaining samples cannot be explained through these two models. Samples 33 and 22 are affected by air contamination (Figure 5a); sample 20 and 26 are consistent with a binary mixing between the ASW and different phases defined by Model 2 (light blue stars in Figure 5a). For instance, sample 20 lies along the mixing line between ASW and phase PA (mixing line 1, Figure 5a), defined by Model 2 and composed by 4.85×10^{-2} mol kg^{-1} of CO_2, 7.47×10^{-8} mol kg^{-1} of He and 6.99×10^{-6} mol kg^{-1} of Ar; sample 26 is consistent with mixing between the ASW and phase PB (mixing line 2, Figure 5a), composed by 5.40×10^{-2} mol kg^{-1} of CO_2, 2.58×10^{-8} mol kg^{-1} of He and 2.36×10^{-6} mol kg^{-1} of Ar.

4.5. Evolution of Inorganic Carbon Dissolved in Groundwaters

To unravel the source of CO_2 dissolved in the Eifel-Ardennes-Rhenish Massif groundwaters, the isotopic composition of the dissolved inorganic carbon ($\delta^{13}C_{TDIC}$, 13 new data, 34 literature data, Ricci et al., 2026) was investigated. Figure 6 displays the external carbon (C_{ext}) and the $\delta^{13}C$ of external carbon ($\delta^{13}C_{ext}$) dissolved in groundwaters compared to the theoretical models (Model 1, Model 2 and Model 3) described in Section 4.4. C_{ext} is the fraction of TDIC derived from sources external to the aquifer and is computed according to Chiodini et al. (2000) and Frondini et al. (2019) as follows:

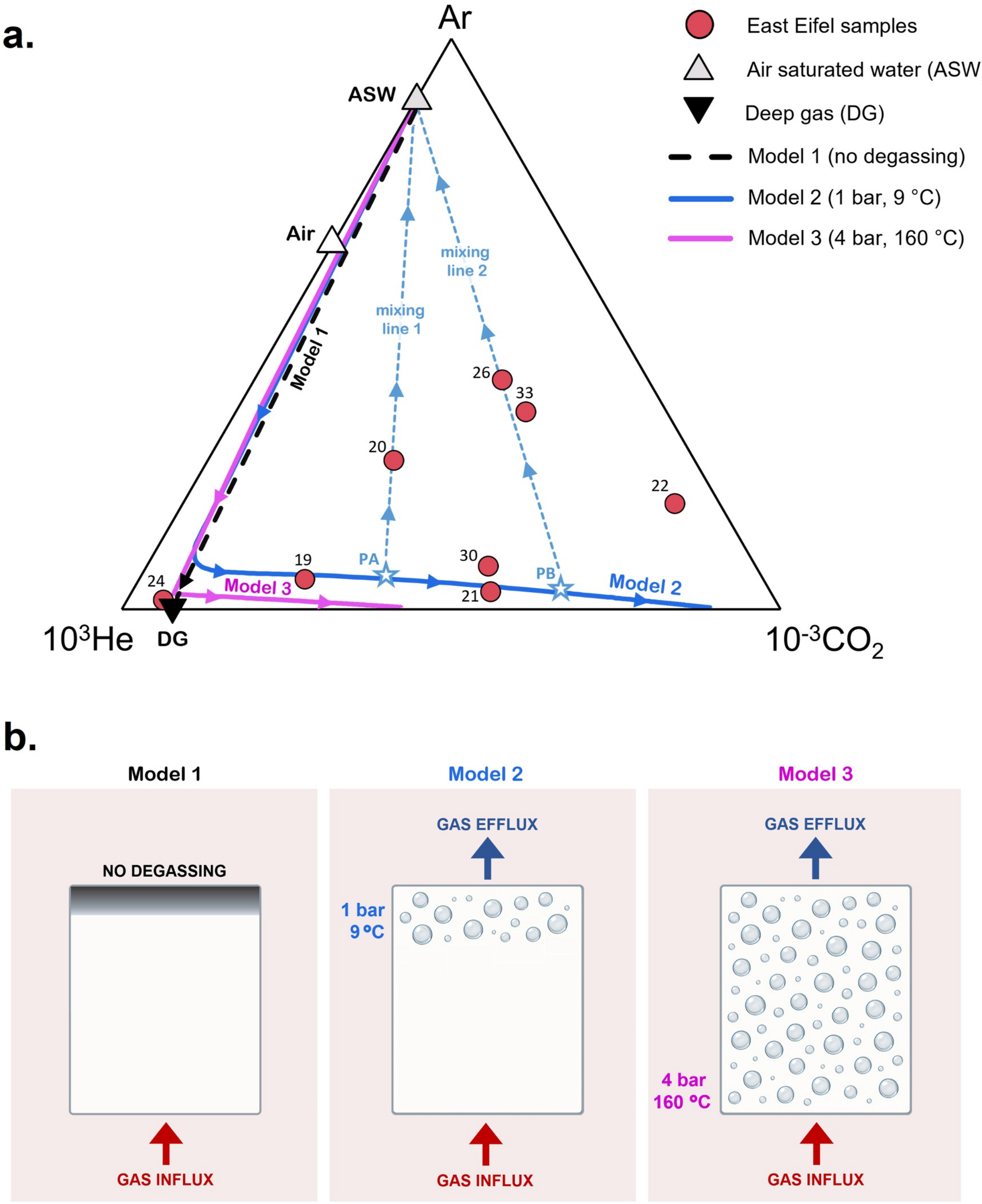

Figure 5. (a) He-Ar-CO_2 ternary diagram, showing the composition of East Eifel samples, air saturated water, air, deep gas and the evolution trends predicted by Model 1 (dashed black line), Model 2 (blue line) and Model 3 (pink line). The diagram also shows the theoretical phases PA and PB (light blue stars) and the mixing lines 1 and 2 (dotted light blue lines); (b) conceptual illustration of the three theoretical models.

$$C_{ext} = TDIC - C_{carb} \tag{1}$$

where C_{carb} is the amount of dissolved carbon supplied by carbonate mineral dissolution, given by

$$C_{carb} = mCa + mMg - mSO_4 \tag{2}$$

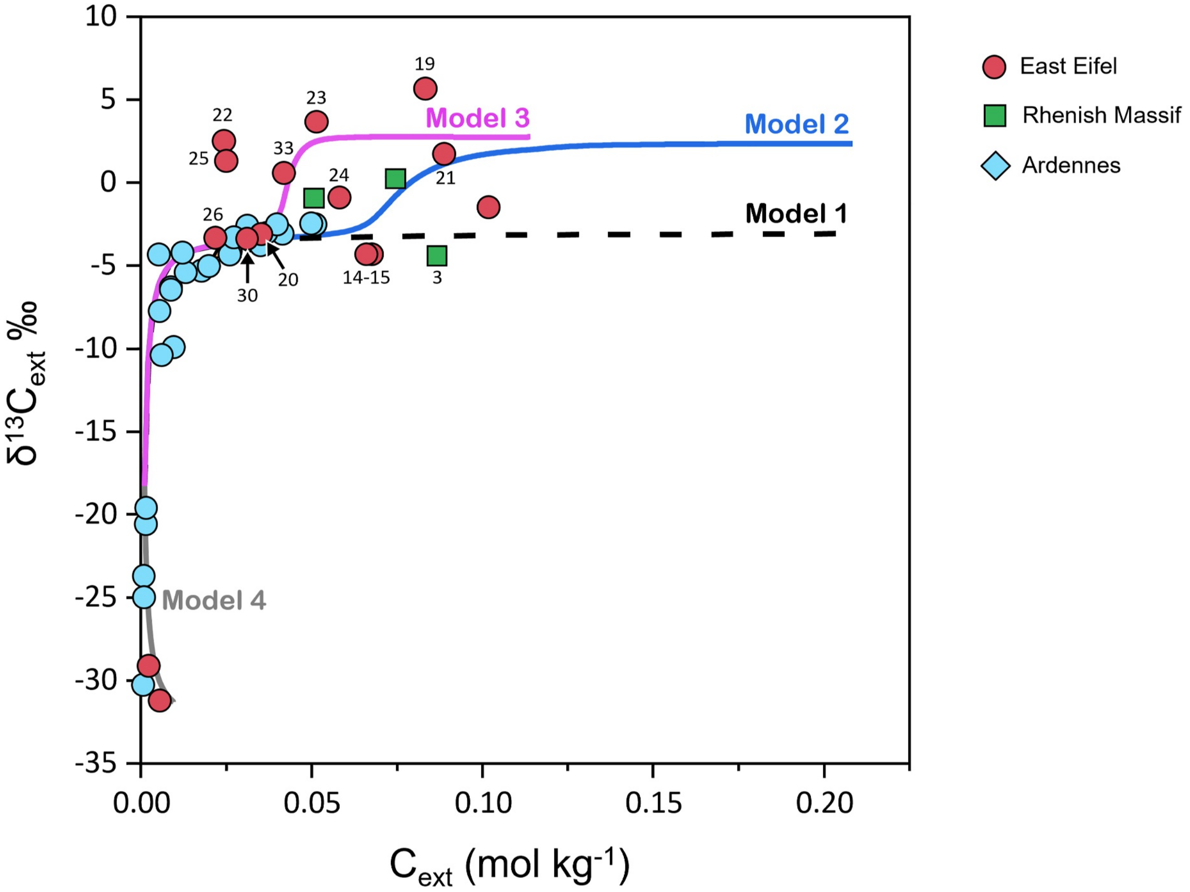

Figure 6. $\delta^{13}C_{ext}$–C_{ext} plot of the studied springs. The theoretical evolution of groundwaters as computed by Model 1 (dashed black curve), Model 2 (blue curve), Model 3 (pink curve) and Model 4 (gray curve) is also shown (see text).

In Equation 2, mCa, mMg and mSO_4 are, respectively, the moles of dissolved calcium, magnesium and sulfate in each water system.

The corresponding $\delta^{13}C_{ext}$ is computed by

$$\delta^{13}C_{ext} = \left(\delta^{13}C_{TDIC} - \delta^{13}C_{carb} \times \frac{C_{carb}}{TDIC}\right) \times \frac{TDIC}{C_{ext}} \tag{3}$$

If no carbonate minerals occur in the aquifer(s), the amount of C_{carb} is negligible, leading to

$$C_{ext} = TDIC \tag{4}$$

and

$$\delta^{13}C_{ext} = \delta^{13}C_{TDIC} \tag{5}$$

For the other systems, the $\delta^{13}C_{ext}$ is determined by Equation 3, using $\delta^{13}C_{carb}$ equals to +1.4‰ (average $\delta^{13}C$ of the Mediterranean Eocene-Oligocene carbonates, Bodiselitsch et al., 2004; Cornacchia et al., 2018).

Samples emerging from the East Eifel and the Rhenish Massif *sensu strictu* do not require any correction of the TDIC by removal of the C_{carb}, since these waters circulate on volcanic and/or metamorphic-siliciclastic lithologies, where carbonate-bearing minerals (e.g., limestones) are rare or absent. Therefore, for these solutions, C_{carb} is equal to zero and C_{ext} corresponds to the TDIC. Carbonate occurrence in Ardennes host rocks is challenging to assess. In-sequence thrusting models of the Ardennes predict carbonates (Devono-Carboniferous limestones outcropping to the northern Ardennes) below the Stavelot-Venn Massif (from which Spa, Bru and Malmedy springs emerge) at a depth of 2–6 km (Barros et al., 2021 and references therein), while out-of-sequence thrust propagation models confine carbonates to the north of the Massif (Barros et al., 2021). To evaluate both scenarios, the C_{carb} for Ardennes waters was computed (Ricci et al., 2026). It is noteworthy that the computed C_{carb} contents are low, constituting less than 10% of the TDIC for most samples and reaching 20%–25% of the TDIC only for three samples (samples 124, 131 and 141). This leads to minimal variations in the computed $\delta^{13}C_{ext}$, resulting similar to the $\delta^{13}C_{TDIC}$ for most samples.

The three theoretical models shown in Figure 6 (and defined in Section 4.4) simulate the evolution of an infiltrating water that progressively interacts with a mantle-sourced CO_2-rich gas phase. The carbon content of the infiltrating water (C_{inf}) and its isotopic composition ($\delta^{13}C_{inf}$) are assumed to be equal to the C_{ext} and the $\delta^{13}C_{ext}$ of Sop water (sample 124; 8.54×10^{-4} mol kg^{-1} and −23.71‰, respectively). This sample is assessed to be representative of the infiltrating water considering the low ^{13}C content and the low C_{ext}, both suggesting the absence of any C_{deep} inputs (Chiodini et al., 2000).

The isotopic composition of the DG ($\delta^{13}C_{deep}$) is set to −3‰, as the $\delta^{13}C$ signature of the free gaseous phase ($\delta^{13}C_{CO2}$) measured at Laacher See (R/Ra = 5.4, Bräuer et al., 2013). Model 1 evolves following a hyperbolic trend, asymptotic to the $\delta^{13}C_{deep}$ value (−3‰). Model 2 retraces the trend of Model 1 up to $C_{ext} = 1.25 \times 10^{-2}$ mol kg^{-1} and $\delta^{13}C_{ext} = -4.33$‰, then, when the solution reaches the saturation with CO_2, it starts to degas carbon dioxide. This induces a shift toward higher $\delta^{13}C_{ext}$ than those predicted by Model 1, reaching $\delta^{13}C_{ext} = +2.34$‰ at the end of the simulation. Model 3 has the same trend as Model 2, but the shift toward higher $\delta^{13}C_{ext}$ begins at $C_{ext} = 3.12 \times 10^{-2}$ mol kg^{-1}, $\delta^{13}C_{ext} = -3.53$‰ and $\delta^{13}C_{ext}$ of +2.77‰ is reached by the end of the simulation.

The majority of samples plot along Model 2 and Model 3 or between them. Most of Ardennes samples can be explained by all the 3 models, since they plot where the models are practically coincident. Four samples from the East Eifel (samples 19, 22, 23 and 25) are not constrained by the three models, since they show much positive $\delta^{13}C_{ext}$ than those predicted by the models. Two East Eifel waters (samples 31 and 32) and five Ardennes samples located at Spa (samples 124, 126 and 129) and at Bru (samples 131 and 132) show strongly negative values of $\delta^{13}C_{ext}$, lower than −19.5‰, suggesting (a) the absence of any deep C source and (b) the contribution of organic carbon. These data are in agreement with a model that simulates the interaction between the infiltrating water and organic carbon (Model 4, gray line in Figure 6) performed by adding 0.0085 mol of organic carbon (C_{bio}) with a carbon isotopic composition ($\delta^{13}C_{bio}$) of −28‰ (Chiodini et al., 2000 and references therein) to the infiltrating water in 100 steps.

4.6. Computation of the Deep Carbon Flux

The total dissolved inorganic carbon (TDIC), the partial pressure of CO_2 (pCO_2) and the calcite saturation index ($SI_{calcite}$) of springwaters were computed by performing aqueous speciation of each solution through the PHREEQC version 3 code and the results are reported in Ricci et al. (2026). To reconstruct the original carbon content at aquifer conditions, the TDIC of samples that, at sampling conditions, are oversaturated with calcite ($SI_{calcite} > 0$) were re-computed with increasing pCO_2 until the equilibrium with calcite is achieved. The resulting *Computed Total Dissolved Inorganic Carbon*, $TDIC_c$, represents the total carbon content of each solution under aquifer conditions. For samples that, at emergence, are in equilibrium or undersaturated with calcite ($SI_{calcite} \leq 0$), TDIC is equal to $TDIC_c$. The deeply derived carbon ($C_{deep,c}$) is computed following Ricci et al. (2024) by the equation:

$$C_{deep,c} = C_{ext,c} - C_{inf} \tag{6}$$

where $C_{ext,c}$ is computed as follows:

$$C_{ext,c} = TDIC_c - C_{carb} \tag{7}$$

Results of $TDIC_c$, $C_{ext,c}$ and $C_{deep,c}$ for each springwater are listed in Ricci et al. (2026) and a statistical description of these parameters is provided in Supporting Information S1.

The average CO_2 flux in the Eifel-Ardennes-Rhenish Massif area can be estimated by means of the following equations:

$$fCO_2 = \eta C_{deep,c} \times I \times \varepsilon \tag{8}$$

and

$$I = \mu P \times EIC \tag{9}$$

where $\eta C_{deep,c}$ is the median of $C_{deep,c}$ (3.59×10^{-2} mol kg^{-1}, 95% CI [2.87×10^{-2}; 4.50×10^{-2} mol kg^{-1}]), I is the infiltration, μP (mm/yr) is the mean annual precipitation, EIC is the effective infiltration coefficient, an empirical, dimensionless parameter depending on the lithology and expressing the percentage of precipitation that infiltrates at depth (Rossi & Donnini, 2018) and ε is the factor needed to convert I from mm to L km^{-2} ($\varepsilon = 10^6$).

To properly apply Equations 8 and 9, some hydrological and lithological observations are required. The mean annual precipitation over the area is lower on the eastern side (East Eifel, 596–658 mm/yr, Meersmans et al., 2016; Stumpp et al., 2014) and increases westward (West Eifel, e.g., 724–872 mm/yr, Meersmans et al., 2016; Stumpp et al., 2014; Steinritz et al., 2024 and references therein), reaching highest values in the Ardennes (1,100–1,200 mm/yr, Meersmans et al., 2016). The average annual precipitation μP is 848 ± 216 mm/year.

The average EIC determination requires further considerations. The Rhenish Massif, made of sandstones, schists and slates, is characterized by low permeability and limited porosity. According to literature data for similar lithologies (metamorphic/sedimentary terrains), the EIC can be considered to be 0.08–0.18 (Duda et al., 2006; Patil et al., 2019; Stako et al., 2012), in agreement with Herrmann et al. (2015). The Volcanic Eifel displays a variety of volcanic formations, from lava flows to lapilli fallout deposits (Schmincke, 2007) characterized by different permeabilities. Although volcanic terrains generally exhibit higher EIC (e.g., EIC of 0.3 for Italian volcanic provinces, Rossi & Donnini, 2018; EIC of 0.3–0.5 for the highly vesicular and fractured basalts of Infranz catchment area, Ethiopia, Nigate et al., 2020), it is noteworthy the Eifel volcanics stack on the Rhenish shield. Water circulation, enhanced by structural discontinuities, extends beyond the shallow volcanic layers, involving the basement. In addition, the strong erosion characterizing West Eifel (Schmincke, 2007) also favors the infilling of rainwater through the metamorphic formations of the Rhenish Massif rather than through the volcanic deposits. Hence, the EIC in the Volcanic Eifel is likely comparable to that of the Rhenish Massif (EIC ∼ 0.1–0.2). In the Ardennes, dominant lithologies involve low-grade metamorphic rocks (schists, slates, quartzites) and sedimentary deposits (sandstones and limestones). As stated by Barros et al. (2021), the main water storage is in the fractured/faulted quartzites (Barros et al., 2021), where permeability can be considered on average not high, except for areas of extensive fracture systems (Rossi & Donnini, 2018). According to the estimations performed on similar lithologies (metamorphic rocks/sandstones, Duda et al., 2006; Patil et al., 2019; Stako et al., 2012), Ardennes EIC can be considered to be of ∼0.1–0.2, similar to that characterizing the Rhenish shield.

Based on the aforementioned observations, we considered a value of 0.15 as a proper average EIC for the study area.

The application of Equations 8 and 9 provides an average deeply derived CO_2 flux of $5 \pm 2 \times 10^6$ mol yr^{-1} km^{-2}.

A rough estimation of the total CO_2 emission rate (rC_{deep}) from the study area can be given by

$$rC_{deep} = fCO_2 \times S \tag{10}$$

where S is the surface extension of the study area (1,600 ± 160 km^2), computing a rC_{deep} of $7 \pm 4 \times 10^9$ mol yr^{-1}.

5. Discussion

5.1. Origin of Fluids

The Eifel-Ardennes-Rhenish Massif springwaters originate from the infiltration of meteoric water, as inferred by the $\delta^{18}O$-δD diagram (Figure 3), with the addition of a deep gas phase, mainly deriving from the mantle. He

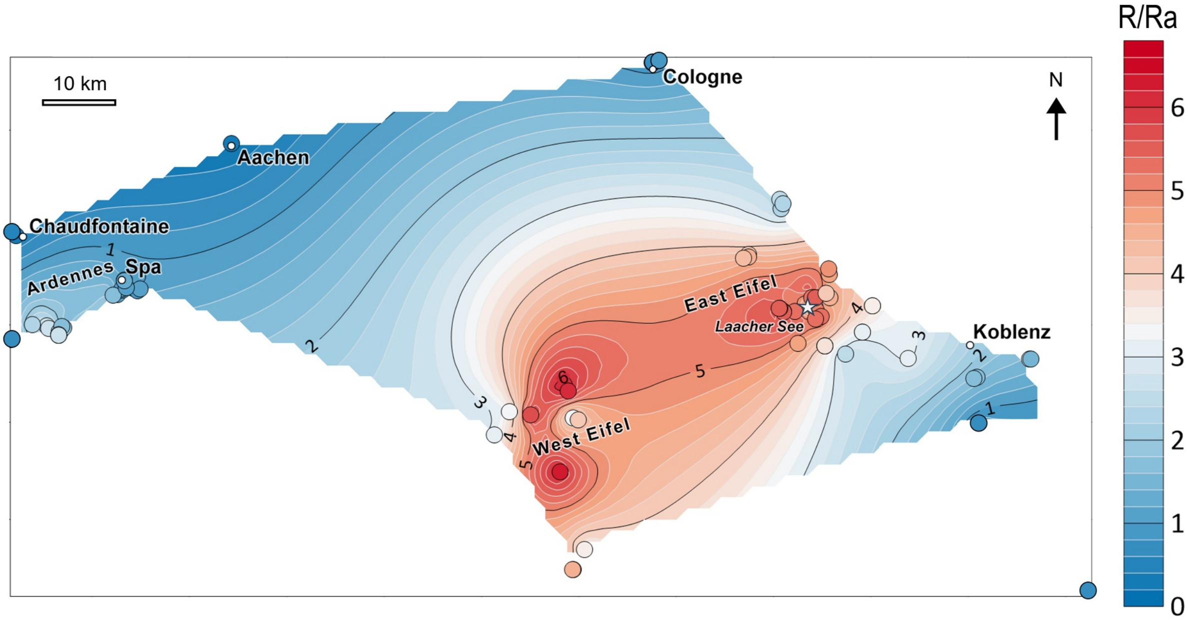

Figure 7. Spatial distribution of R/Ra ratio in springwaters emerging at the East Eifel (Bekaert et al., 2019; Bräuer et al., 2013; Griesshaber et al., 1992), the Rhenish Massif *sensu strictu* (Bräuer et al., 2013; Griesshaber et al., 1992) and the Ardennes regions (Defourny et al., 2022; Griesshaber et al., 1992), in Laacher See lake (Giggenbach et al., 1991) and in fluid inclusions from West Eifel (Rizzo et al., 2021).

isotope distribution in groundwaters (Bekaert et al., 2019; Bräuer et al., 2013; Defourny et al., 2022; Griesshaber et al., 1992; Figure 7), Laacher See lake (Giggenbach et al., 1991) and in fluid inclusions (Rizzo et al., 2021 and references therein) shows an intriguing spatial variability in the ^{3}He/^{4}He ratio. In the Volcanic Eifel, R/Ra (where R stands for the ^{3}He/^{4}He ratio in the sample and Ra is the ^{3}He/^{4}He ratio of atmosphere, equals to 1.38×10^{-6}, Clarke et al., 1976) is between 4 and 6.8 (Bekaert et al., 2019; Bräuer et al., 2013; Giggenbach et al., 1991; Griesshaber et al., 1992; Rizzo et al., 2021 and references therein), in the range of the typical signature of the subcontinental lithospheric mantle ($R/Ra = 6.1 \pm 0.9$, Gautheron & Moreira, 2002; $R/Ra = 6.1 \pm 2.1$, Day et al., 2015) and congruent with the R/Ra ratio measured in fluids from other ECRIS sectors (French Massif Central, Boudoire et al., 2023; Eger Rift, Daskalopoulou et al., 2025). Highest ratios characterize fluids escaping in the surrounding of Laacher See and Wehr volcanoes (R/Ra between 5.2 and 5.6, Bräuer et al., 2013; Giggenbach et al., 1991; Griesshaber et al., 1992) and fluid inclusions from West Eifel (R/Ra from 5.5 to 6.8, Rizzo et al., 2021). Ardennes show lower ratios (R/Ra from 0.2 to 2.8, Defourny et al., 2022; Griesshaber et al., 1992), while fluids emerging from the Rhenish Massif *sensu strictu* encompasses a wider R/Ra range, between 0.8 and 4.9 (Bräuer et al., 2013; Griesshaber et al., 1992). This indicates mixing of the mantle source with a crustal component ($R/Ra = 0.05$, Andrews, 1985) and/or with atmospheric gases ($R/Ra = 1$, by definition). Such spatial distribution suggests Volcanic Eifel, Ardennes and Rhenish Massif *sensu strictu* may belong to a unique degassing system, with Volcanic Eifel (where fluids show up to 74% of mantle–He, Griesshaber et al., 1992) as the core and the Ardennes (where crustal–He is between 50% and 80%, Defourny et al., 2022) and Rhenish Massif *sensu strictu* (mantle–He between 8% and 57%, Griesshaber et al., 1992) as the peripheral areas of the degassing structure. These findings reinforce the observations of Defourny et al. (2022), who previously suggested a link between the Ardennes and the Volcanic Eifel by combining δ^{13}C and He/CO$_2$ data.

The Langelier-Ludwig diagram (Figure 2c), supported by the salinity section (Figure 2d) and the HCO$_3$-TDS binary plot (Figure 2a), highlights that springwaters are the result of mixing between low-mineralized, shallow-circulating waters and highly mineralized fluids associated with the deep hydrothermal system. The latter are: (a) the Rhenish Massif *sensu strictu* groundwaters, which preserve a marked thermal footprint at emergence, showing the highest TDS of the entire data set and being characterized by sodium-chloride or sodium-bicarbonate composition and (b) Aechean springs (sample 155 to 161), hydrothermal waters with Na-Cl composition and high TDS (~4,000 mg L^{-1}), whose maturity suggests long residence times. Major fault systems from which these springs emerge have a key role in enhancing the circulation at depth, allowing the imprint of the hydrothermal features and the rising at the surface.

The good correlation between bicarbonate and the Total Dissolved Solids (Figure 2a) hints that bicarbonate concentration is a major driver of water salinity and this is easily explained considering the behavior of bicarbonate in water as a weak acid, enhancing the dissolution of the surrounding rocks.

Both East and West Eifel waters (with exception of sample 53) lie in the bicarbonate field of the Langelier-Ludwig diagram (Figure 2c), spanning the bicarbonate-Earth alkaline and the bicarbonate-alkaline composition. Considering the alkaline chemistry of Eifel volcanics and the high CO_2 content of these springwaters (pCO_2 up to 2 bars; CO_2% vol in the free gas up to 99.8%, Bräuer et al., 2013), the dissolution of volcanic glass driven by carbonic acid is the main mechanism acting in these areas. The high concentration of dissolved CO_2 prevents the attainment of the equilibrium, which explains why East and West Eifel waters are immature. Andernach (samples 13) might be considered the most representative of the "deep East Eifel aquifer" (Figures 2c and 2d). Andernach is the world's highest cold geyser (height comprises between 30 and 60 m), fed by a 350 m-depth artesian well and emerging at the intersection of two major fault systems: the NE-SW Siegen Thrust Fault and the NW-SE Andernach fault (Bornemann et al., 2020), constituting the pathway for gas ascent (Bornemann et al., 2020). Ardennes waters, on the other hand, plot in the bicarbonate-Earth alkaline sector (Figure 2c), consistent with the lithologies occurring in the area (slates, quartzites, sandstones). Although Ardennes show a weak tendency toward the Na-Cl vertex and therefore toward Aachen waters, the salinity section and the HCO_3-TDS diagram clearly indicate that Ardennes and Aachen systems are the result of distinct processes that led to a different water composition.

Theoretical models of water-gas-rock interaction that simulate the evolution of a meteoric water progressively interacting with a mantle-derived, CO_2-rich gas phase and degassing CO_2 at the surface (Model 2, $P = 1$ bar) and/or at aquifer conditions (Model 3, $P = 4$ bar) constrain the chemical and isotopic composition of most of the studied samples (Figures 5 and 6).

The shift affecting the trend of Model 2 and Model 3 (Figure 6) is due to CO_2 degassing, occurring when oversaturation with CO_2 is achieved. In fact, the separation of a new phase is accompanied by isotopic fractionation, which makes the heavier phase (i.e., water) enriched in the heavier nuclides (^{13}C), while ^{12}C leaves the system with the gaseous phase (i.e., degassed CO_2).

Neither Model 2, nor Model 3 can explain the isotopic composition of external carbon of four samples from the East Eifel (samples 19, 22, 23 and 25), since they show much positive $\delta^{13}C_{ext}$ than those predicted by the theoretical models. These compositions would be constrained only considering a heavier C of mantle CO_2, with $\delta^{13}C$ up to −1‰. This is in contrast with free gas data, where $\delta^{13}C_{CO2}$ is between −6.3 and −3‰ at East Eifel (Bräuer et al., 2013) and is up to −2‰ only in the southern side of West Eifel (Bräuer et al., 2013). Isotopic measurements of $\delta^{13}C_{CO2}$ in fluid inclusions entrapped in mantle xenoliths would be required to shed a light on the pristine isotopic composition of mantle C beneath the Eifel region.

Finally, Figure 6 displays the theoretical models based on East Eifel data and also predicts the C_{ext} and the $\delta^{13}C_{ext}$ composition of Ardennes springwaters. This result corroborates the hypothesis of Defourny et al. (2022), which suggests that mantle gas escaping from the Ardennes and the Volcanic Eifel has a common origin. The lower R/Ra ratios measured in the Ardennes (Figure 7), together with lower % of mantle He in the gas phase (from 12% to 35%, Barros et al., 2021; Griesshaber et al., 1992), suggest that Ardennes volatiles may be a mix of mantle and crustal/atmospheric gases, while Eifel fluids preserve the mantle footprint. Fluids with mantellic markers mainly occur where magma dikes rise (i.e., in the Volcanic Eifel); moving away from the eruptive centers, the magmatic signature becomes diluted, since the deep fluids rising through the oblique sub-lithospheric faults mix with crustal and, ultimately, with atmospheric gases, explaining the lower values measured, for instance, in the Ardennes.

5.2. CO_2 Budget

The average deeply derived CO_2 flux here computed for the Eifel-Ardennes-Rhenish Massif area is $5 \pm 2 \times 10^6$ mol yr^{-1} km^{-2} and the total deeply sourced CO_2 emission rate is $7 \pm 4 \times 10^9$ mol yr^{-1}. The CO_2 emission rate is one order of magnitude higher than (a) the CO_2 degassing estimated from West Eifel (3.7×10^8 mol yr^{-1}, May, 2002) and (b) the CO_2 degassing estimated ($1.1 \pm 0.3 \times 10^8$ mol yr^{-1}, Aeschbach-Hertig et al., 1996) and measured ($2.9 \pm 0.1 \times 10^8$ mol yr^{-1}, Pérez et al., 2011) at Laacher See. Therefore, the CO_2 annually emitted from the Laacher See would account for just 4% of the total emission rate from the Eifel-Ardennes-Rhenish Massif region. On the other hand, it is worth noting that the specific CO_2 flux from the Laacher

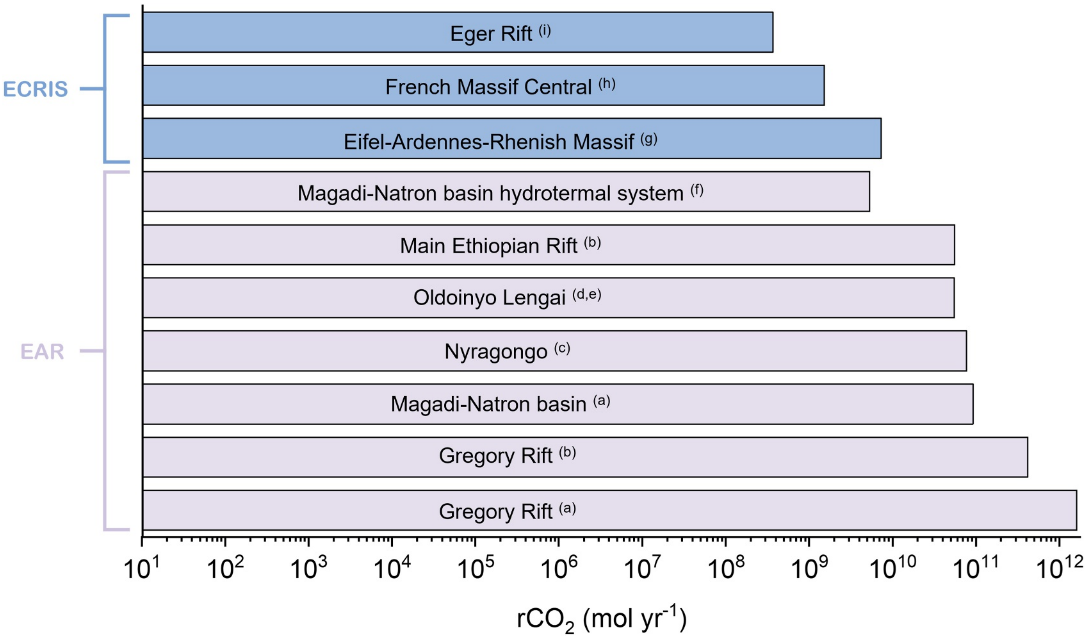

Figure 8. Comparison of the total CO_2 emission rates (rCO_2) from active (East African Rift, EAR) and passive rifts (European Cenozoic Rift System, ECRIS). Data are from (a) Lee et al. (2016), (b) Hunt et al. (2017), (c) Sawyer et al. (2008), (d) Brantley and Koepenick (1995), (e) Fischer et al. (2009), (f) Lee et al. (2017), (g) this work, (h) Ricci et al. (2024), and (i) Weinlich et al. (1999).

See (1.2×10^8 mol yr^{-1} km^{-2}, Pérez et al., 2011), which considers the surface area from which the outgassing occurs (2.5 km^2), is two orders of magnitude higher than the average flux here computed from the whole region ($5 \pm 2 \times 10^6$ mol yr^{-1} km^{-2}, surface area of 1,600 km^2). According to Dahm et al. (2020), the largest CO_2 reservoir of East Eifel might be at Wehr (~1 km westward the Laacher See), where 1.8×10^9 mol yr^{-1} are produced from CARBO industries (Dahm et al., 2020 and references therein). Our data confirm the neighboring of Laacher See (e.g., Wehr, Rieden, Plaidt) is affected by strong CO_2 transport through groundwaters (with $C_{deep,c}$ up to 2.52×10^{-1} mol kg^{-1}), but similar deep C contents can be found in the Rhenish Massif *sensu strictu* (e.g., at Bad Honnef). Similarly to what can be observed in the French Massif Central (Ricci et al., 2024), CO_2 degassing from the Eifel-Ardennes-Rhenish Massif area is strongly driven by the tectonics, with fractures and/or faults favoring the rise of mantle CO_2, even in the absence of volcanism. The deeply sourced CO_2 emission rate from the Eifel-Ardennes-Rhenish Massif area is of the same order of magnitude than those computed at the French Massif Central ($1.52 \pm 0.14 \times 10^9$ mol yr^{-1}, Ricci et al., 2024) and one order of magnitude higher than the emission rate in the western Eger rift (3.6×10^8 mol yr^{-1}). This points to a slight spatial variability in the extent of the outgassing within the ECRIS system. These values are from the same to four orders of magnitude lower than the CO_2 emission rates measured or estimated along the East African Rift (Figure 8), whose surface area is about two order of magnitude higher than the Eifel-Ardennes-Rhenish Massif and the French Massif Central regions: 5.31×10^9 mol yr^{-1} at the Magadi-Natron hydrothermal system (Lee et al., 2017); 7.7×10^{10} mol yr^{-1} from the Nyragongo (Sawyer et al., 2008); 5.5×10^{10} mol yr^{-1} from the Oldoinyo Lengai (Brantley & Koepenick, 1995; Fischer et al., 2009); 5.5×10^{10} mol yr^{-1} at the Main Ethiopian Rift (Hunt et al., 2017); 9.2×10^{10} mol yr^{-1} at the Magadi-Natron basin (Lee et al., 2016); 0.9–7.4×10^{11} mol yr^{-1} (Hunt et al., 2017) and 1.6×10^{12} mol yr^{-1} (Lee et al., 2016) from the Gregory Rift (eastern branch of the East African Rift).

6. Conclusions

This paper provides the first regional estimation of the deep CO_2 emission rate transported by groundwaters in the Eifel-Ardennes-Rhenish Massif area ($7 \pm 4 \times 10^9$ mol yr^{-1}), corresponding to a flux of $5 \pm 2 \times 10^6$ mol yr^{-1} km^{-2}. This value is of the same magnitude as the global CO_2 flux baseline characterizing geothermal regions (10^6 mol yr^{-1} km^{-2}, Kerrick et al., 1995). Between 45% and 85% of the total deep carbon rising from the mantle and transported toward the surface by groundwaters is released in the atmosphere and/or precipitated as calcite. This highlights the relevance of CO_2 degassing from passive rifts in the evaluation of the endogenous Earth CO_2

outgassing, which remains one order of magnitude lower than the degassing affecting active rifts (0.26–1 × 10^7 mol yr^{-1} km^{-2}, Hunt et al., 2017; Lee et al., 2016). We also determine, for the first time, the chemistry of East Eifel dissolved gases, which allows us to unravel the dynamics of the degassing process. Groundwaters underwent CO_2 release between aquifer depth (4 bar, 160°C) and spring emergence (1 bar, 9°C). The isotopic evolution of dissolved carbon and the spatial distribution of He isotopes reveal that the Ardennes, Volcanic Eifel and Rhenish Massif are part of a unique degassing system. This evidence, previously suggested by Defourny et al. (2022), is demonstrated here through theoretical degassing models based on East Eifel geochemistry, which also constrain the carbon isotopic signature of the Ardennes and Rhenish Massif groundwaters. We propose that tectonic structures are the main pathway for CO_2 rise and transport in the region. The existence of a continuous S-E dipping reflector, extending from the Ardennes to the Volcanic Eifel with a minimum length of 80 km (Eickhoff et al., 2025) supports our scenario. Furthermore, these reflecting zones have a low impedance contrast that may indicate the occurrence of fluids within the Eifel Fold and Thrust Belt (Eickhoff et al., 2025).

Conflict of Interest

The authors declare no conflicts of interest relevant to this study.

Availability Statement

The Eifel-Ardennes-Rhenish Massif data set and the Carbon Mass Balance calculations are available on the Zenodo repository (Ricci et al., 2026).

Acknowledgments

This work was funded by the MUR-PRIN Projects: PRIN2017 – 2017LMNLAW “Connect4Carbon” and PRIN2022 – 2022HA8XCS “CRUSCA.” Open access publishing facilitated by Universita degli Studi di Perugia, as part of the Wiley - CRUI-CARE agreement.

References

Aeschbach-Hertig, W., Kipfer, R., Hofer, M., Imboden, D. M., Wieler, R., & Signer, P. (1996). Quantification of gas fluxes from the subcontinental mantle: The example of Laacher See, a maar lake in Germany. *Geochimica et Cosmochimica Acta*, *60*(1), 31–41. https://doi.org/10.1016/0016-7037(95)00370-3

Andrews, J. N. (1985). The isotopic composition of radiogenic helium and its use to study groundwater movement in confined aquifers. *Chemical Geology*, *49*(1–3), 339–351. https://doi.org/10.1016/0009-2541(85)90166-4

Aulbach, S., Lin, A.-B., Weiss, Y., & Yaxley, G. M. (2020). Wehrlites from continental mantle monitor the passage and degassing of carbonated melts. *Geochemical Perspectives Letters*, *15*, 30–34. https://doi.org/10.7185/geochemlet.2031

Barros, R., Defourny, A., Collignon, A., Jobe, P., Dassargues, A., Piessens, K., & Welkenhuysen, K. (2021). A review of the geology and origin of CO_2 in mineral water springs in east Belgium. *Geologica Belgica*, *24*(1–2), 17–31. https://doi.org/10.20341/gb.2020.023

Bekaert, D. V., Broadley, M. W., Caracausi, A., & Marty, B. (2019). Novel insights into the degassing history of Earth's mantle from high precision noble gas analysis of magmatic gas. *Earth and Planetary Science Letters*, *525*, 115766. https://doi.org/10.1016/j.epsl.2019.115766

Bodiselitsch, B., Montanari, A., Koeberl, C., & Coccioni, R. (2004). Delayed climate cooling in the late Eocene caused by multiple impacts: High-resolution geochemical studies at Massignano, Italy. *Earth and Planetary Science Letters*, *223*(3–4), 283–302. https://doi.org/10.1016/j.epsl.2004.04.028

Bornemann, T. L. V., Adam, P. S., Turzynski, V., Schreiber, U., Figueroa-Gonzalez, P. A., Rahlff, J., et al. (2020). Geological degassing enhances microbial metabolism in the continental subsurface [preprint]. *bioRxiv*. https://doi.org/10.1101/2020.03.07.980714

Boudoire, G., Gailler, L., Battaglia, J., Beauger, A., Bontemps, M., Bosse, V., et al. (2025). Scientific response to the 2021–2022 seismic swarm in the Monts Dore volcanic province (France): Dynamic insights from temporal surveys (2/2). *Comptes Rendus Geoscience*, *357*(G1), 79–103. https://doi.org/10.5802/crgeos.285

Boudoire, G., Pasdeloup, G., Schiavi, F., Cluzel, N., Rafflin, V., Grassa, F., et al. (2023). Magma storage and degassing beneath the youngest volcanoes of the Massif Central (France): Lessons for the monitoring of a dormant volcanic province. *Chemical Geology*, *634*, 121603. https://doi.org/10.1016/j.chemgeo.2023.121603

Brantley, S. L., & Koepenick, K. W. (1995). Measured carbon dioxide emissions from Oldoinyo Lengai and the skewed distribution of passive volcanic fluxes. *Geology*, *23*(10), 933–936. https://doi.org/10.1130/0091-7613(1995)023<0933:MCDEFO>2.3.CO;2

Bräuer, K., Kämpf, H., Niedermann, S., & Strauck, G. (2013). Indications for the existence of different magmatic reservoirs beneath the Eifel area (Germany): A multi-isotope (C, N, He, Ne, Ar) approach. *Chemical Geology*, *356*, 193–208. https://doi.org/10.1016/j.chemgeo.2013.08.013

Brune, S., Williams, S. E., & Müller, R. D. (2019). Potential links between continental rifting, CO_2 degassing and climate change through time. *Nature Geoscience*, *10*(12), 941–946. https://doi.org/10.1038/s41561-017-0003-6

Caliro, S., Chiodini, G., Avino, R., Cardellini, C., & Frondini, F. (2005). Volcanic degassing at Somma-Vesuvio (Italy) inferred by chemical and isotopic signatures of groundwaters. *Applied Geochemistry*, *20*(6), 1060–1076. https://doi.org/10.1016/j.apgeochem.2005.02.002

Cappelli, L., Wallace, P. A., Randazzo, A., Kamau, P. M., Njoroge, R. W., Otieno, V., et al. (2023). Diffuse soil CO_2 emissions at rift volcanoes: Structural controls and total budget of the Olkaria Volcanic Complex (Kenya) case study. *Journal of Volcanology and Geothermal Research*, *443*, 107929. https://doi.org/10.1016/j.jvolgeores.2023.107929

Caracausi, A., Avice, G., Burnard, P. G., Füri, E., & Marty, B. (2016). Chondritic xenon in the Earth’s mantle. *Nature*, *533*(7601), 82–85. https://doi.org/10.1038/nature17434

Chiodini, G. (1996). Gases dissolved in groundwaters: Analytical methods and examples of applications in central Italy. In *Proceedings of the Rome Seminar on Environmental Geochemistry, Castelnuovo di Porto, 22–26 May 1996* (pp. 135–148).

Chiodini, G., Frondini, F., Cardellini, C., Parello, F., & Peruzzi, L. (2000). Rate of diffuse carbon dioxide Earth degassing estimated from carbon balance of regional aquifers: The case of central Apennine, Italy. *Journal of Geophysical Research*, *105*(B4), 8423–8434. https://doi.org/10.1029/1999JB900355

Clarke, W. B., Jenkins, W. J., & Top, Z. (1976). Determination of tritium by mass spectrometric measurements of ^{3}He. *The International Journal of Applied Radiation and Isotopes*, *27*(9), 5115–5522. https://doi.org/10.1016/0020-708X(76)90082-X

Climate Change Knowledge Portal. (2025). Retrieved from https://climateknowledgeportal.worldbank.org/

Cornacchia, A., Brandano, M., Raffi, I., Tomassetti, L., & Flores, I. (2018). The Eocene–Oligocene transition in the C-isotope record of the carbonate successions in the Central Mediterranean. *Global and Planetary Change*, *167*, 110–122. https://doi.org/10.1016/j.gloplacha.2018.05.012

Craig, H. (1961). Isotopic variations in meteoric waters. *Science*, *133*(3465), 1702–1703. https://doi.org/10.1126/science.133.3465.1702

Dahm, T., Stiller, M., Mechie, J., Heimann, S., Hensch, M., Woith, H., et al. (2020). Seismological and geophysical signatures of the deep crustal magma systems of the Cenozoic volcanic fields beneath the Eifel, Germany. *Geochemistry, Geophysics, Geosystems*, *21*(9), e2020GC009062. https://doi.org/10.1029/2020GC009062

Dansgaard, W. (1964). Stable isotopes in precipitation. *Tellus*, *16*(4), 436–468. https://doi.org/10.1111/j.2153-3490.1964.tb00181.x

Daskalopoulou, K., Niedermann, S., Wilke, F. D. H., Zimmer, M., Woith, H., Glodny, J., et al. (2025). Characterisation of deep intra-continental magma reservoirs – Insights from noble gases and *p-T* estimates into the western Eger Rift (Czech Republic). *Chemical Geology*, *681*, 122722. https://doi.org/10.1016/j.chemgeo.2025.122722

Day, J. M. D., Barry, P. H., Hilton, D. R., Burgess, R., Pearsoon, G., & Taylor, L. A. (2015). The helium flux from the continents and ubiquity of low-^{3}He/^{4}He recycled crust and lithosphere. *Geochimica et Cosmochimica Acta*, *153*, 116–133. https://doi.org/10.1016/j.gca.2015.01.008

Defourny, A., Blard, P.-H., Zimmermann, L., Jobé, P., Collignon, A., Nguyen, F., & Dassargues, A. (2022). δ^{13}C, CO_2/^{3}He and ^{3}He/^{4}He ratios reveal the presence of mantle gas in the CO_2-rich groundwaters of the Ardennes massif (Spa, Belgium). *Hydrology and Earth Sciences*, *26*(10), 2637–2648. https://doi.org/10.5194/hess-26-2637-2022

DEKORP Research Group. (1991). Results of the DEKORP 1 (BELCORP-DEKORP) deep seismic reflection studies in the western part of the Rhenish Massif. *Geophysical Journal International*, *106*(1), 203–227. https://doi.org/10.1111/j.1365-246X.1991.tb04612.x

Delany, J. M., & Lundeen, S. R. (1990). *The LLNL thermochemical database* (p. 150). Lawrence Livermore National Laboratory Report UCRL21658.

Demoulin, A. (1998). Testing the tectonic significance of some parameters of longitudinal river profiles: The case of the Ardenne (Belgium, NW Europe). *Geomorphology*, *24*(2–3), 189–208. https://doi.org/10.1016/S0169-555X(98)00016-6

Dèzes, P., Schmid, S. M., & Ziegler, P. A. (2004). Evolution of the European Cenozoic Rift System: Interaction of the Alpine and Pyrenean orogens with their foreland lithosphere. *Tectonophysics*, *389*(1–2), 1–33. https://doi.org/10.1016/j.tecto.2004.06.011

Duda, A., & Schmincke, H.-U. (1985). Polybaric differentiation of alkali basaltic magmas: Evidence from green-core clinopyroxenes (Eifel, FRG). *Contributions to Mineralogy and Petrology*, *91*(4), 340–353. https://doi.org/10.1007/BF00374690

Duda, R., Zdechlik, R., & Paszkiewicz, M. (2006). Some remarks on numerical modelling of the Rava River basin. *Geologos*, *10*, 47–56.

Eickhoff, D., Back, S., Reicherter, K., & Ritter, J. R. R. (2025). Seismic reprocessing of BELCORP-DEKORP 1A reveals deep fault reflections of the Paleozoic Eifel Fold and Thrust Belt in Germany. *Tectonophysics*, *903*, 230702. https://doi.org/10.1016/j.tecto.2025.230702

Fischer, T. P., Burnard, P., Marty, B., Hilton, D. R., Füri, E., Palhol, F., et al. (2009). Upper-mantle volatile chemistry at Oldoinyo Lengai volcano and the origin of carbonatites. *Nature*, *459*(7243), 77–80. https://doi.org/10.1038/nature07977

Fournier, R. O., & Potter II, R. W. (1982). A revised and expanded silica (quartz) geothermometer. *Geothermal Resources Council Bulletin*, *11*, 3–12.

Frondini, F., Cardellini, C., Caliro, S., Beddini, G., Rosiello, A., & Chiodini, G. (2019). Measuring and interpreting CO_2 fluxes at regional scale: The case of the Appennines, Italy. *Journal of the Geological Society*, *176*(2), 408–416. https://doi.org/10.1144/jgs2017-169

Gal, F., Leconte, S., & Gafalia, A. (2018). The "Escarot" gas seep, French Massif Central: CO_2 discharge from a quiescent volcanic system – Characterization and quantification of gas emissions. *Journal of Volcanology and Geothermal Research*, *353*, 68–82. https://doi.org/10.1016/j.jvolgeores.2018.01.026

Gautheron, C., & Moreira, M. (2002). Helium signature of the subcontinental lithospheric mantle. *Earth and Planetary Science Letters*, *199*(1–2), 39–47. https://doi.org/10.1016/S0012-821X(02)00563-0

Giggenbach, W. F. (1988). Geothermal solute equilibria. Derivation of Na-K-Mg-Na geoindicators. *Geochimica et Cosmochimica Acta*, *52*(12), 2749–2765. https://doi.org/10.1016/0016-7037(88)90143-3

Giggenbach, W. F., & Goguel, R. L. (1989). *Collection and analysis of geothermal and volcanic water and gas discharges*. Report No. CD 2401. Chemistry Division, DSIR.

Giggenbach, W. F., Sano, Y., & Schmincke, H. U. (1991). CO_2-rich gases from Lakes Nyos and Monoun, Cameroon; Laacher See, Germany; Dieng, Indonesia, and Mt Gambier, Australia-variations on a common theme. *Journal of Volcanology and Geothermal Research*, *45*(3–4), 311–323. https://doi.org/10.1016/0377-0273(91)90065-8

Gómez-Díaz, E., Morales, A. B., Kukla, P. A., & Brehme, M. (2025). Integrative analysis of the aachen geothermal system (Germany) with an interdisciplinary conceptual model. *Geothermal Energy*, *13*(1), 7. https://doi.org/10.1186/s40517-024-00327-0

Griesshaber, E., O'Nions, R. K., & Oxburgh, E. R. (1992). Helium and carbon isotope systematics in crustal fluids from the Eifel, the Rhine Graben and Blak Forest, F.R.G. *Chemical Geology*, *99*(4), 213–235. https://doi.org/10.1016/0009-2541(92)90178-8

Hence, L., Dejonghe, L., Ghysel, P., Laloux, M., & Mansy, J. L. (1999). Influence of heterogeneous lithostructural layering on orogenic deformation in the Variscan Front Zone (eastern Belgium). *Tectonophysics*, *309*(1–4), 161–177. https://doi.org/10.1016/S0040-1951(99)00137-7

Herrmann, F., Keller, L., Kunkel, R., Vereecken, H., & Wendland, F. (2015). Determination of spatially differentiated water balance components including groundwater recharge on the Federal State level – A case study using the mGROWA model in North Rhine-Westphalia (Germany). *Journal of Hydrology: Regional Studies*, *4*, 294–312. https://doi.org/10.1016/j.ejrh.2015.06.018

Hunger, H.-J., Tichomirowa, M., Jöns, N., Mollenhauer, G., Grotheer, H., Gent, T., et al. (2024). Contribution to the eruption mechanism of carbonatitic diatremes and volcanoes. *Geology, Earth and Marine Sciences*, *6*(7), 11–13.

Hunt, J. A., Zafu, A., Mather, T. A., Pyle, D. M., & Barry, P. H. (2017). Spatially variable CO_2 degassing in the Main Ethiopian Rift: Implications for magma storage, volatile transport, and rift-related emissions. *Geochemistry, Geophysics, Geosystems*, *18*(10), 3714–3737. https://doi.org/10.1002/2017GC006975

Illies, J. H., & Greiner, G. (1979). Holocene movements and state if stress in the Rhinegraben rift system. *Tectonophysics*, *52*(1–4), 349–359.

Kämpf, H., Broge, A. S., Marzban, P., Allahbakhshi, M., & Nickschick, T. (2019). Nonvolcanic carbon dioxide emission at continental rifts: The Bublak Mofette Area, Western Eger Rift, Czech Republic. *Geofluids*, *2019*, 1–19. https://doi.org/10.1155/2019/4852706

Kern, Z., Hatvani, I. G., Czuppon, G., Fórizs, I., Erdélyi, D., Kanduč, T., et al. (2020). Isotopic 'altitude' and 'continental' effects in modern precipitation across the Adriatic–Pannonian region. *Water*, *12*(6), 1797. https://doi.org/10.3390/w12061797

Kerrick, D. M., McKibben, M. A., Seward, T. M., & Caldeira, K. (1995). Convective hydrothermal CO_2 emission from high heat flow regions. *Chemical Geology*, *121*(1–4), 285–293. https://doi.org/10.1016/0009-2541(94)00148-2

Krämer, M., Schüle, M., & Schütz, L. (1996). A method to determine rainwater solutes from pH and conductivity measurements. *Atmospheric Environment*, *30*(19), 3291–3300. https://doi.org/10.1016/1352-2310(96)00070-2

Langelier, W., & Ludwig, H. (1942). Graphical methods for indicating the mineral character of natural waters. *American Water Works Association*, *34*(3), 335–352. https://doi.org/10.1002/j.1551-8833.1942.tb19682.x

Lee, H., Fischer, T. P., Muirhead, J. D., Ebinger, C. J., Kattenhorn, S. A., Sharp, Z. D., et al. (2017). Incipient rifting accompanied by the release of subcontinental lithospheric mantle volatiles in the Magadi and Natron basin, East Africa. *Journal of Volcanology and Geothermal Research*, *346*, 118–133. https://doi.org/10.1016/j.jvolgeores.2017.03.017

Lee, H., Muirhead, J. D., Fischer, T. P., Ebinger, C. J., Kattenhorn, S. A., Sharp, Z. D., & Kianji, G. (2016). Massive and prolonged deep carbon emissions associated with continental rifting. *Nature Geoscience*, *9*(2), 145–149. https://doi.org/10.1038/ngeo2622

May, F. (2002). Säuerlinge der Vulkaneifel und der Südeifel. *Mainzer Geowissenschaftliche Mitteilungen*, *31*, 7–58. https://doi.org/10.23689/fidgeo-5740

May, F., Hoernes, S., & Neugebauer, H. J. (1996). Genesis and distribution of mineral waters as a consequence of recent lithospheric dynamics: The Rhenish Massif, Central Europe. *Geologische Rundschau*, *85*(4), 782–799. https://doi.org/10.1007/s005310050112

Meersmans, J., Van Weverberg, K., De Baets, S., De Ridder, F., Palmer, S. J., van Wasemael, B., & Quine, T. (2016). Mapping mean total precipitation in Belgium, by investigating the scale of topographic control at the regional scale. *Journal of Hydrology*, *540*, 96–105. https://doi.org/10.1016/j.jhydrol.2016.06.013

Mertes, H., & Schmincke, H.-U. (1985). Mafic potassic lavas of the Quaternary West Eifel volcanic field. *Contributions to Mineralogy and Petrology*, *89*(4), 330–345. https://doi.org/10.1007/bf00381555

Moreira, M., Rouchon, V., Muller, E., & Noirez, S. (2018). The xenon isotopic signature of the mantle beneath Massif Central. *Geochemical Perspectives Letters*, *6*, 28–32. https://doi.org/10.7185/geochemlet.1805

Nigate, F., Van Camp, M., Yenehun, A., Belay, A. S., & Walraevens, K. (2020). Recharge–discharge relations of groundwater in volcanic terrain of semi-humid tropical highlands of Ethiopia: The case of Infranz Springs, in the Upper Blue Nile. *Water*, *12*(3), 853. https://doi.org/10.3390/w12030853

Parkhurst, D. L., & Appelo, C. A. J. (2013). Description of input and examples for PHREEQC version 3—A computer program for speciation, batch-reaction, one-dimensional transport, and inverse geochemical calculations. *US Geological Survey Techniques and Methods*, *6*(A43), 497. https://doi.org/10.3133/tm6A43

Patil, M., Saha, A., Karwariya, S., Pingale, S. M., Goyal, V. C., Rathore, D. S., & Behera, N. (2019). Assessment of rainfall recharge using rainfall infiltration factor method and empirical equations. *Discovery Nature*, *13*, 1–8.

Pérez, N. M., Hernández, P. A., Padilla, G., Nolasco, D., Barrancos, J., Melian, G., et al. (2011). Global CO_2 emission from volcanic lakes. *Geology*, *39*(3), 235–238. https://doi.org/10.1130/G31586.1

Pfahl, S., & Sodemann, H. (2014). What controls deuterium excess in global precipitation? *Climate of the Past*, *10*(2), 771–781. https://doi.org/10.5194/cp-10-771-2014

Rafflin, V., Boudoire, G., Massaro, S., Stocchi, M., Costa, A., Grassa, F., et al. (2024). Modelling CO_2 dispersion in the air during potential limnic eruption at the lake Pavin (France). *Journal of Volcanology and Geothermal Research*, *447*, 108024. https://doi.org/10.1016/j.jvolgeores.2024.108024

Ricci, L., Frondini, F., Morgavi, D., Caliro, S., Rizzo, A. L., Fischer, T. P., & Chiodini, G. (2026). The Eifel-Ardennes-Rhenish Massif Dataset and Carbon Mass Balance Calculations [Dataset]. *Zenodo*. https://doi.org/10.5281/zenodo.19551103

Ricci, L., Frondini, F., Morgavi, D., Vetuschi Zuccolini, M., Boudoire, G., Laumonier, M., et al. (2024). CO_2 flux from the French Massif Central groundwaters: Modelling and quantitative estimation of the degassing process. *Chemical Geology*, *652*, 122012. https://doi.org/10.1016/j.chemgeo.2024.122012

Riley, T. R., Bailey, D. K., Harmer, R. E., Liebsch, H., Lloyd, F. E., & Palmer, M. R. (1999). Isotopic and geochemical investigation of a carbonatite-syenite-phonolite diatreme, West Eifel (Germany). *Mineralogical Magazine*, *63*(5), 615–631. https://doi.org/10.1180/002646199548736

Riley, T. R., Bailey, D. K., & Lloyd, F. E. (1996). Extrusive carbonatite from the Quaternary Rockeskyll complex, West Eifel, Germany. *The Canadian Mineralogist*, *34*(2), 389–403.

Ritter, J. R. R., Jordan, M., Christensen, U. R., & Achauer, U. (2001). A mantle plume below the Eifel volcanic fields, Germany. *Earth and Planetary Science Letters*, *186*(1), 7–14. https://doi.org/10.1016/S0012-821X(01)00226-6

Ritter, J. R. R., Koushesh, K., Schmidt, B., Föst, J.-P., Bühler, J., Hensch, M., & Mader, S. M. (2024). Seismological monitoring of magmatic and tectonic earthquakes in the East Eifel Volcanic Field, Germany. *Journal of Seismology*, *28*(6), 1325–1350. https://doi.org/10.1007/s10950-024-10257-w

Rizzo, A. L., Faccini, B., Casetta, F., Faccincani, L., Ntaflos, T., Italiano, F., & Coltorti, M. (2021). Melting and metasomatism in West Eifel and Siebengebirge Sub-Continental Lithospheric Mantle: Evidence from concentrations of volatiles in fluid inclusions and petrology of ultramafic xenoliths. *Chemical Geology*, *581*, 120400. https://doi.org/10.1016/j.chemgeo.2021.120400

Romano, P., & Liotta, M. (2020). Using and abusing Giggenbach ternary Na-K-Mg diagram. *Chemical Geology*, *541*, 119577. https://doi.org/10.1016/j.chemgeo.2020.119577

Rossi, M., & Donnini, M. (2018). Estimation of regional scale effective infiltration using an open source hydrogeological balance model and free/open data. *Environmental Modelling & Software*, *104*, 153–170. https://doi.org/10.1016/j.envsoft.2018.03.005

Sawyer, G. M., Carn, S. A., Tsanev, V. I., Oppenheimer, C., & Burton, M. (2008). Investigation into magma degassing at Nyiragongo volcano, Democratic Republic of the Congo. *Geochemistry, Geophysics, Geosystems*, *9*(2), Q02017. https://doi.org/10.1029/2007GC001829

Schmincke, H. U. (2007). The Quaternary volcanic fields of the East and West Eifel (Germany). In J. R. R. Ritter & U. R. Christensen (Eds.), *Mantle plumes* (pp. 241–322). Springer. https://doi.org/10.1007/978-3-540-68046-8_8

Schmincke, H.-U., Lorenz, V., & Seck, H. A. (1983). The Quaternary Eifel volcanic fields. In K. Fuchs, K. V. Gehlen, H. Mälzer, H. Murawski, & A. Semmel (Eds.), *Plateau uplift: The Rhenish Shield - A case history* (pp. 139–151). Springer.

Schmincke, H.-U., Park, C., & Harms, E. (1999). Evolution and environmental impacts of the eruption of Laacher See Volcano (Germany) 12,900 a BP. *Quaternary International*, *61*(1), 61–72. https://doi.org/10.1016/S1040-6182(99)00017-8

Schmitt, A. K., Klitzke, M., Gerdes, A., & Schäfer, C. (2017). Zircon hafnium-oxygen isotope and trace element petrochronology of intraplate volcanic rocks from the Eifel (Germany) and implications for mantle versus crustal origins of zircon megacrysts. *Journal of Petrology*, *58*(9), 1841–1870. https://doi.org/10.1093/petrology/egx075

Schmitt, A. K., Wetzel, F., Cooper, K. M., Zou, H., & Wörner, G. (2010). Magmatic longevity of Laacher See volcano (Eifel, Germany) indicated by U-Th dating of intrusive carbonatites. *Journal of Petrology*, *51*(5), 1053–1085. https://doi.org/10.1093/petrology/egq011

Schumacher, M. E. (2002). Upper Rhine Graben: The role of preexisting structures during rift evolution. *Tectonics*, *21*(1), 6-1–6-17. https://doi.org/10.1029/2001TC900022

Shaw, C. S. J. (2004). The temporal evolution of three magmatic systems in the West Eifel volcanic field, Germany. *Journal of Volcanology and Geothermal Research*, *131*(3–4), 213–240. https://doi.org/10.1016/S0377-0273(03)00363-9

Shaw, C. S. J., Lebert, B. S., & Woodland, B. (2018). Thermodynamic modelling of mantle-melt interaction evidenced by veined wehrlite xenoliths from the Rockeskyllerkopf Volcanic complex, west Eifel volcanic field. Germany. *Journal of Petrology*, *59*(1), 59–86. https://doi.org/10.1093/petrology/egy018

Stako, S., Tarka, R., & Olichwer, T. (2012). Groundwater recharge evaluation based on the infiltration method. In P. Maloszewski, S. Witczak, & G. Malina (Eds.), *Groundwater quality sustainability* (1st ed.). CRC Press. https://doi.org/10.1201/b12715

Steinritz, V., Bellanova, P., Schmidt, B., Schüttrumpf, H., Schwarzbauer, J., & Reicherter, K. (2024). Geomorphic changes after the 2021 Central European flood in the Ahr Valley by LiDAR-based differences. *Environmental Sciences Europe*, *36*(1), 75. https://doi.org/10.1186/s12302-024-00893-x

Stumpp, C., Klaus, J., & Stichler, W. (2014). Analysis of long-term stable isotopic composition in German precipitation. *Journal of Hydrology*, *517*, 351–361. https://doi.org/10.1016/j.jhydrol.2014.05.034

Sundermeyer, C., Gätjen, J., Weimann, L., & Wörner, G. (2020). Timescales from magma mixing to eruption in alkaline volcanism in the Eifel volcanic fields, western Germany. *Contributions to Mineralogy and Petrology*, *175*(8), 77. https://doi.org/10.1007/s00410-020-01715-y

Tamburello, G., Pondrelli, S., Chiodini, G., & Rouwet, D. (2018). Global-scale control of extensional tectonics on CO_2 earth degassing. *Nature Communications*, *9*(1), 4608. https://doi.org/10.1038/s41467-018-07087-z

Van Daele, J., & Ferket, H. (2021). *CO_2-seeps around the Laacher See [Fact sheet]*. Flemish Planning Bureau for the Environment and Spatial Development (VPO).

Van-Den-Boom, G., & Krimmel, M. (1986). Geochemische Untersuchungen im Gebiet Lehrheim/Lahn unter Verwendung gasförmiger Elemente und Verbindungen. Geologisches Jahrbuch. Reihe D. *Mineralogie, Petrographie, Geochemie, Lagerstättenkunde*, *81*, 1–19.

Van Overmeeren, R. (2014). *Vulkanisme en CO_2 in de Eifel - Geologische (wandel) excursies*. Universiteit Utrecht.

Weinlich, F. H., Bräuer, K., Kämpf, H., Strauch, G., Tesař, J., & Weise, S. M. (1999). An active subcontinental mantle volatile system in the western Eger rift, Central Europe: Gas flux, isotopic (He, C, and N) and compositional fingerprints. *Geochimica et Cosmochimica Acta*, *63*(21), 3653–3671. https://doi.org/10.1016/S0016-7037(99)00187-8

Wolery, T. J. (1979). *Calculation of chemical equilibrium between aqueous solution and minerals- The EQ3/6 software package*. Lawrence Livermore National Laboratory Report UCRL-52658.

Wolery, T. J. (1992). EQ3/EQ6, a software package for geochemical modelling of aqueous systems, package overview and installation guide (version 7.0). Lawrence Livermore National Laboratory Report UCRL-MA110662(1).

Wolery, T. J., & Jarek, R. L. (2003). *EQ3/6, version 8.0—Software User's Manual*. Civilian Radioactive Waste Management System, Management & Operating Contractor. Sandia National Laboratories.

Wörner, G., & Schmincke, H. U. (1984). Mineralogical and chemical zonation of the Laacher See tephra sequence (East Eifel, W. Germany). *Journal of Petrology*, *25*(4), 805–835. https://doi.org/10.1093/petrology/25.4.805

Wörner, G., Viereck, L., Plaumann, S., Pucher, R., van den Bogaard, P., & Schmincke, H. U. (1988). The Quaternary Wehr volcano: A multiphase evolved eruption center in the east Eifel volcanic field (FRG). *Neues Jahrbuch für Mineralogie - Abhandlungen*, *159*(1), 73–99. https://doi.org/10.1127/njma/159/1988/73

Zolitschka, B., Negendank, J. F. W., & Lottermoser, B. G. (1995). Sedimentological proof and dating of the Early Holocene volcanic eruption of Ulmener Maar (Vulkaneifel, Germany). *Geologische Rundschau*, *84*(1), 213–219. https://doi.org/10.1007/BF00192252

References From the Supporting Information

Langguth, H. R., & Plum, H. (1984). *Untersuchung der Mineral-und Thermalquellen der Eifel auf geothermische Indikationen* (p. 196). Technologische Forschung und Entwicklung - Nichtnukleare Energietechnik, Lehr- und Forschungsgebiet für Hydrogeologie der RWTH Aachen, Bundesministerium für Forschung und Technologie. Forschungsbericht, BMFT-FBT 84-019.

Lehnert, K., Su, Y., Langmuir, C. H., Sarbas, B., & Nohl, U. (2000). A global geochemical database structure for rocks. *Geochemistry, Geophysics, Geosystems*, *1*(5), 1012. https://doi.org/10.1029/1999GC000026

Monjoie, A. (1997). Etude des eaux carbogazeuses du sud-est de la Belgique. Grant Spadel internal report 971.

Wasserquellen atlas. (2022a). Bad Bodendorf, St. Josef-Quelle. *Chemical Water Analysis*. Retrieved from https://www.quellenatlas.eu/media/c91ed820c78e6983ffff85ebac14421f.pdf

Wasserquellen atlas. (2022b). Bad Breisig, Geiersprudel. *Chemical Water Analysis*. Retrieved from http://www.quellenatlas.eu/media/b0a59653c5bb8707ffff875cac14422f.pdf

Wasserquellen atlas. (2022c). Bad Neuenahr, Willibrordus-Sprudel, Großer Sprudel. *Chemical Water Analysis*. Retrieved from http://www.quellenatlas.eu/media/ea7a5ab0fc3f3c97ffff814effffffef.pdf

Wasserquellen atlas. (2022d). Bad Tönisstein, Kurfürstenbrunnen und Angelikaquelle. *Chemical Water Analysis*. Retrieved from http://www.quellenatlas.eu/media/3d1a6f3696cc3efffff8123ac144232.pdf

Wasserquellen atlas. (2022e). Bettenfeld Dreisborn. *Chemical Water Analysis*. Retrieved from http://www.quellenatlas.eu/media/51ab0f8b696c8911ffff8049ac14422f.pdf

Wasserquellen atlas. (2022f). Bodenbach Drees. *Chemical Water Analysis*. Retrieved from http://www.quellenatlas.eu/media/44d27c193a8c1015ffff80dcfffffff0.pdf

Wasserquellen atlas. (2022g). Boppard - Bad Salzig Leonorenbrunnen. *Chemical Water Analysis*. Retrieved from http://www.quellenatlas.eu/media/3e204c496990eb7cffff80e4ac14421f.pdf

Wasserquellen atlas. (2022h). Daun Dunaris-Quelle. *Chemical Water Analysis*. Retrieved from http://www.quellenatlas.eu/media/96fa8e139dc0a076ffff805cfffffff1.pdf

Wasserquellen atlas. (2022i). Daun-Steinborn Steema Drees. *Chemical Water Analysis*. Retrieved from http://www.quellenatlas.eu/media/33039aa3c78d810cffff8553ac144232.pdf

Wasserquellen atlas. (2022j). Dockweiler Drees. *Chemical Water Analysis*. Retrieved from https://www.quellenatlas.eu/media/db963bf190181e01ffff804cfffffff0.pdf

Wasserquellen atlas. (2022k). Dreis-Brück Vulkania-Heilquelle. *Chemical Water Analysis*. Retrieved from http://www.quellenatlas.eu/media/33039aa3c78d810cffff8567ac144232.pdf

Wasserquellen atlas. (2022l). Duppach Drees. *Chemical Water Analysis*. Retrieved from http://www.quellenatlas.eu/media/51ab0f8b696c8911ffff8037ac14422f.pdf

Wasserquellen atlas. (2022m). Gerolstein Helenenquelle. *Chemical Water Analysis*. Retrieved from http://www.quellenatlas.eu/media/2b574205c78c63f8ffff8611ac144227.pdf

Wasserquellen atlas. (2022n). Niederstadtfeld Sauerbrunnen. *Chemical Water Analysis*. Retrieved from http://www.quellenatlas.eu/media/a1d8f9ae1dced077ffff98ceac144221.pdf